

## THE GASEOUS ENVIRONMENTS OF POWERFUL EXTENDED RADIO SOURCES

GREG F. WELLMAN, RUTH A. DALY,<sup>1</sup> AND LIN WAN

Department of Physics, Princeton University, Princeton, NJ 08544

Received 1996 July 27; accepted 1996 November 22

### ABSTRACT

The properties of very powerful extended (FR II) radio sources can be used to probe their gaseous environments. In particular, the velocity of lobe propagation and the lobe minimum energy magnetic field may be used to estimate the density of the ambient gas around a given source. A sample of 14 radio galaxies and eight radio-loud quasars with redshifts from 0 to 2 are studied in detail. The radio data are used to estimate the lobe magnetic field and the lobe propagation velocity. These are combined to obtain an estimate of the ambient gas density in the vicinity of the radio lobe using the equation of ram pressure confinement; generally, two densities are obtained for each source, one for each radio lobe. Several possible selection effects are studied in detail, including the power-redshift selection effect that arises from the fact that the sample is flux limited, and the correlation of radio spectral index with redshift.

The key result is that the sources are in gaseous environments similar to those found in low-redshift clusters of galaxies. One of the sources in this study is Cygnus A, and the gaseous environments of the sources studied seem to be similar to that in the vicinity of this low-redshift, very powerful extended radio source. Not only are the typical densities obtained similar to those found in low-redshift clusters, but the composite density profile is as well. Thus, it appears that these sources lie in cluster-like gaseous environments, though the sources are observed out to relatively large redshift, having redshifts between 0 and 2.

There is some evidence that the core density of the gaseous environments about the sources evolves with redshift in the sense that higher redshift systems have lower core gas densities, but the data are consistent with a constant core gas mass model in which the core density decreases and the core radius increases with redshift in such a way that the total core gas mass remains roughly constant. It does not seem likely that this result is related to the radio power-redshift selection effect, but it could be related to the radio spectral index-redshift selection effect, and a study of this and other selection effects is continuing. When a simple correction is applied to account for the radio spectral index-redshift selection effect, the negative evolution of the core gas density with redshift is only significant at about the  $2\sigma$  level.

Several independent observations now indicate that powerful extended radio sources have magnetic field strengths that are lower than estimated minimum energy field strengths. Three independent measures of the offset of the magnetic field from that estimated assuming minimum energy conditions are discussed here and in a companion paper. Consistency between independent measures of the same quantity is obtained if the true magnetic field strength has an offset of about 0.25 from the minimum energy field, a result consistent with that obtained by other groups. In addition, the data presented here can be used to place a limit on the source-to-source dispersion of the offset. It is shown that most sources probably have a very similar offset; the source-to-source dispersion in the offset is likely to be less than about 15%.

*Subject headings:* cosmology: observations — galaxies: active — galaxies: clusters: general — galaxies: intergalactic medium — shock waves

### 1. INTRODUCTION

Powerful extended FR II radio sources are an attractive tool to study cosmology and evolution of structure because they are observed over a broad range of redshift. The nature of the environments of these radio sources as a function of redshift has been considered in a number of studies (see, e.g., Yee & Green 1987; Yates, Miller, & Peacock 1989; Hill & Lilly 1991; Allington-Smith et al. 1993; Wan & Daly 1996a, 1996b; Daly 1995a, 1995b; Wellman & Daly 1996b). Some form of gaseous environment is required by the standard “beam model” (see, e.g., Begelman, Blandford, & Rees 1984 and references therein) of double-lobed radio sources to provide the working surface for the beam to terminate. If

the source has a very small lobe-lobe separation, the gas is likely to be the interstellar medium (ISM) of the host galaxy. At core-lobe separations greater than about  $25 h^{-1}$  kpc, such as those considered here, the gas is likely to be the intracluster medium (ICM) or intergalactic medium (IGM), depending on whether the source is in a cluster or the field; throughout the paper, Hubble’s constant is taken to be  $H_0 = 100 h \text{ km s}^{-1} \text{ Mpc}^{-1}$ , the deceleration parameter is taken to be  $q_0 = 0$  except where  $q_0 = 0.5$  is explicitly considered, and the cosmological constant is taken to be zero. Note also that the “lobe” refers to the roughly spherical radio-emitting region about the radio hot spot, and the “bridge” refers to the radio-emitting region that extends from the radio lobe to the radio core or center of the galaxy or quasar.

X-ray observations of the gaseous environments of nearby radio sources have been obtained and studied in

<sup>1</sup> National Young Investigator.

detail (see, e.g., Fabbiano et al. 1979; Burns, Gregory, & Holman 1981; Vallée & Bridle 1982; Morganti et al. 1988; Burns et al. 1994). Most powerful radio sources, those with 178 MHz powers  $P_{178} > 10^{27} h^{-2} \text{ W Hz}^{-1} \text{ sr}^{-1}$ , lie beyond a redshift of  $\sim 0.5$ , where the resolution of current X-ray instruments generally makes it very difficult to unambiguously determine whether the emission, when detected, is extended or nuclear (see Henry & Henriksen 1986; Crawford & Fabian 1993, 1995; Worrall et al. 1994; Sokolowski, Daly, & Lilly 1996). The gaseous environment of Cygnus A, by far the closest radio sources with  $P_{178} > 10^{27} h^{-2} \text{ W Hz}^{-1} \text{ sr}^{-1}$ , has been studied using X-ray observations (see, e.g., Arnaud et al. 1984, 1987; Carilli, Perley, & Harris 1994).

It is possible to estimate the ambient gas density (as a single parameter) in the vicinity of the lobes of powerful extended radio sources from radio data by applying the equation of ram pressure confinement, as was done by Daly (1994, 1995a). This method of estimating the ambient gas density is attractive because it can be applied to powerful FR II radio sources at any redshift for which high resolution multifrequency radio maps exist, and it does not suffer from the uncertainties that plague estimates from X-ray measurements at high redshifts (i.e., the difficulty in distinguishing extended emission from nuclear emission and/or determining the size of the extended component).

In this paper, spectral aging studies of very powerful ( $P_{178} > 10^{27} h^{-2} \text{ W Hz}^{-1} \text{ sr}^{-1}$ ) FR II radio sources are used to derive ambient gas densities at the ends of the lobes; those densities are used to study the gaseous environments of the sources and their redshift evolution. This is an attractive method of estimating the ambient gas density because it yields the density directly, unlike X-ray observations, Faraday rotation and depolarization studies, and Sunyaev-Zeldovich studies, each of which produces the product of the density and other quantities such as the core radius, the gas temperature, and the magnetic field strength.

The paper is structured as follows. The model of source-environment interaction is described and the derivation of the minimum energy magnetic field is reviewed in § 2. The sample is described in § 3, while § 4 describes the data analysis including sources cut from the sample, raw data measurement, the derivation of ages, lobe propagation velocities, and ambient gas densities. An offset from minimum energy conditions is discussed in § 4.2 and the deconvolution procedure in § 4.3. The error analysis is presented in § 5, and the results of fitting the density estimates to theoretical forms to determine a composite density profile are given in § 6. The results are discussed further in § 7, including the effects of selection, projection, and the assumed cosmology. Random deviations from minimum energy conditions are discussed in § 7.4. Conclusions follow in § 8.

## 2. THE MODEL

The standard “beam model” for double-lobed radio sources has been discussed by many authors (see, e.g., Begelman et al. 1984 and references therein). The AGN emits two collimated beams in opposite directions. Each beam powers a driven shock wave through the ambient medium and deposits its energy as relativistic electrons and magnetic field behind the shock. Those electrons then spiral in the magnetic field emitting synchrotron radiation. At 178 MHz radio powers greater than about ( $10^{26}$ – $10^{27}$ )  $h^{-2} \text{ W}$

$\text{Hz}^{-1} \text{ sr}^{-1}$ , radio sources have a straight, regular bridge structure, indicating little or no backflow (see, e.g., Leahy & Williams 1984; Alexander & Leahy 1987). Hence, the measured lobe velocity  $v_L$  must be near the true lobe advance velocity  $v_t$ , where  $v_L = v_t + v_{\text{backflow}}$ , and all velocities are measured relative to the radio core or central region of the host galaxy or quasar. The velocity  $v_L$  is typically estimated to be a few  $10^4 \text{ km s}^{-1}$  (see, e.g., Alexander & Leahy 1987; Liu, Pooley, & Riley 1992, hereafter LPR92; Daly 1994, 1995a), which is much larger than the sound speed in the IGM, ICM, or ISM since the sound speed is typically  $\lesssim 10^3 \text{ km s}^{-1}$ . This led Daly (1994, 1995a) to propose a power cut of  $P_{178} > (10^{26} \text{ to } 10^{27}) h^{-2} \text{ W Hz}^{-1} \text{ sr}^{-1}$  for the use of radio sources as astrophysical or cosmological tools to ensure that the lobe advance is supersonic and  $v_L \simeq v_{\text{true}}$ . This is supported by the study of bridge structures by Wellman & Daly (1996a) and Wellman, Daly, & Wan (1997, hereafter WDW97), which suggests that backflow and particle reacceleration to relativistic energies is insignificant in these sources.

The issue of whether backflow is important in powerful extended radio sources has been discussed recently by Scheuer (1995, 1996). He examined the arm- or lobe-length asymmetry of a sample of powerful radio sources, reported that the growth speeds of the lobes are likely to be less than about 0.15 the speed of light, and estimated that the true velocities are probably a few percent of the speed of light. The bound and most probable velocities obtained by Scheuer (1995, 1996) are consistent with the lobe propagation velocities estimated here using a standard synchrotron and inverse-Compton aging model and with the velocities obtained by Daly (1994, 1995a) using the sample of Leahy, Muxlow, & Stephens (1989, hereafter LMS89). Thus, it appears that any backflow velocity in the sources studied here is likely to be small relative to the true lobe propagation velocity. A numerical comparison between the results of Scheuer (1995, 1996) and the velocities presented here is detailed in the companion paper of WDW97. In addition, as described in WDW97, combining the Mach number of lobe advance with the lobe propagation velocity estimated using the synchrotron and inverse-Compton aging model for Cygnus A yields a prediction of the ambient gas temperature that matches the temperature indicated by X-ray measurements, which also suggests that the velocity estimated using a standard aging model assuming negligible backflow provides a good rough estimate of the true lobe propagation velocity.

Scheuer (1995, 1996) compared his results with some lobe propagation velocities of LPR92, noted that the growth speeds derived from spectral aging for some sources are much larger than that derived from source asymmetry, and thus concluded that backflow must be important in these sources. As described above, the velocities we obtain here and those obtained by Daly (1994, 1995a) using a standard synchrotron and inverse-Compton aging model are completely consistent with those obtained by Scheuer, which indicates that backflow is unlikely to be important in the sources studied here. It is interesting to note that little backflow is also consistent with implications based on observations of bridge shape and structure of powerful radio sources (Alexander & Leahy 1987; Carilli et al. 1991).

In the case of supersonic lobe propagation, the strong shock jump conditions can be applied to the driven shock wave at the end of the lobe. Note that the equation of ram pressure confinement may be applied either to the radio hot

spot or to the radio lobe using the hot spot or lobe propagation velocity, respectively, as discussed in detail by Daly (1995a); here, the equation is applied to the radio lobe. If the minimum energy magnetic field of the lobes is a good approximation to the true field strength, or if deviations from minimum energy are similar from source to source such that all sources are offset from minimum energy conditions by a constant factor (a result suggested in § 7.4), the lobe pressure is proportional to the square of the minimum energy magnetic field. In this case, one of the strong shock jump conditions, known as the equation of ram pressure confinement, implies that

$$n_a \propto (B/v_L)^2, \quad (1)$$

where  $n_a$  is the ambient gas number density and  $B$  is the minimum energy magnetic field of the lobe; this equation was shown by Daly (1994, 1995a, 1995b) to give a reasonable estimate of the ambient gas density in the vicinity of powerful extended (FR II) radio sources. Note that it is rare that the radio data allow an estimate of the hot spot propagation velocity but often allow an estimate of the lobe propagation velocity; thus, the lobe propagation velocity is used here to estimate the ambient gas density. In a few unusual cases, such as Cygnus A, very high resolution radio data allow an estimate of the hot spot propagation velocity, though it is not possible to estimate the hot spot velocity using the samples considered here.

In the case of the simple morphology of the high-power sources, a synchrotron aging analysis is straightforward and yields the speed at which the bridge is lengthening (see Pacholczyk 1970; Jaffe & Perola 1973; Meyer & Spangler 1985; Alexander & Leahy 1987; Alexander 1987; LMS89; Carilli et al. 1991; and LPR92 for discussions and examples). The lobe propagation velocity  $v_L$  is defined as  $\Delta x/\Delta t$ , where  $\Delta x$  is the physical length of some significant portion of the bridge and  $\Delta t$  is the increase in synchrotron and inverse-Compton age across that length. The synchrotron age is a function of the observed break frequency,  $\nu_T$  (the location of the break in the emission spectrum), and is given by the equation (Jaffe & Perola 1973; LPR92)

$$t = \left[ \frac{27\pi e m_e c B}{\sigma_T^2 (B^2 + B_{\text{MWB}}^2) \nu_T} \right]^{1/2},$$

in cgs units or

$$t = 50.2 \frac{B^{1/2}}{B^2 + B_{\text{MWB}}^2} \nu_T^{-1/2}, \quad (2)$$

where  $t$  is in Myr,  $B$  and  $B_{\text{MWB}}$  are in  $10 \mu\text{G}$ , and  $\nu_T$  is in GHz,  $B_{\text{MWB}} = 3.18(1+z)^2 \mu\text{G}$  is the equivalent magnetic field strength of the cosmic microwave background (Jaffe & Perola 1973; LMS89). The break frequency is found by fitting a model-dependent spectrum to the observed multi-frequency data. The two commonly used spectral models are the Kardachev-Pacholczyk (KP) model that assumes no electron pitch angle scattering (Pacholczyk 1970) and the JP model that does assume electron pitch angle isotropization on a timescale short compared with the radiation lifetime (Jaffe & Perola 1973). Most current work uses the JP model because fast pitch angle scattering is considered more physically plausible. However, see Tribble (1993) for a discussion of modifications to the JP and KP models. In the present work, we consider both JP and KP models and find that the results are not sensitive to the

model chosen. Further, the modifications discussed by Tribble (1993) do not affect the results presented here.

It should be pointed out that the standard spectral aging analysis has been under debate recently. Several authors have argued that synchrotron aging may not be the proper or only explanation for the spectral curvature observed in radio sources (Katz-Stone, Rudnick, & Anderson 1993; Rudnick, Katz-Stone, & Anderson 1994; Rudnick & Katz-Stone 1996; Eilek & Arendt 1996; Eilek 1996). Until more conclusive data can be obtained to settle the controversy, we adopt the view that the standard aging analysis can be performed with reasonable confidence. As noted above, the velocities and temperatures obtained using the standard aging analysis agree well with results from lobe asymmetry analysis and X-ray observations, which suggests that this analysis yields a good rough estimate.

### 2.1. Minimum Energy Magnetic Field

Magnetic field strengths are needed for equations (1) and (2). The appropriate location within the source at which to estimate the field for the purpose of applying equation (1) is the lobe, because  $B^2$  in equation (1) is an estimate of the average lobe pressure driving the shock.

Determining the magnetic field to use for the purpose of applying equation (2) is more complicated because the minimum energy magnetic field generally decreases with distance from the hot spot owing to adiabatic losses associated with the lateral expansion of the bridge (e.g., WDW97). Alexander (1987) pointed out that, under some conditions, there is an accidental near-cancellation between the effect of expansion on the electron energy distribution and the decreasing magnetic field, such that using the observed break frequency and the initial (preexpansion) magnetic field will give the correct age to within a reasonable error. However, the effectiveness of the near-cancellation depends upon the assumption that the lateral expansion of the bridge is linear with distance from the hot spot and that inverse-Compton cooling is not a significant contribution to aging. In this sample, it appears from the maps that the expansion history is often nonlinear, usually with faster expansion immediately following the hot spot and slower expansion farther from the hot spot (Wellman & Daly 1996a; WDW97). The data agree with the theoretical models of Begelman & Cioffi (1989) and Daly (1990) who independently derive a relation of the form  $v_{\text{exp}} \propto t^{-1/2}$ . In addition, many sources are at high redshift where inverse-Compton scattering of microwave background photons may contribute to the aging of the electron energy distribution if there is a departure from minimum energy conditions such as that discussed in § 4.2. Considering these uncertainties in determining the synchrotron age, we decided to use a magnetic field that would be an average of the lobe and bridge field and to include uncertainties due to the adiabatic expansion of the bridge in the lateral direction (see §§ 4 and 5 for more details.)

The normal procedure for the aging analyses is to use the minimum energy magnetic field. The standard formula (Miley 1980) was used, assuming no relativistic protons ( $k=0$ ), a filling factor of unity ( $\eta=1$ ), a tangled field (average  $\phi$ , the angle between the source magnetic field and the line of sight, over a sphere), cylindrical symmetry with random orientation (the line-of-sight depth,  $l$ , is taken as  $4/\pi$  times the source width) and a power-law spectrum with cutoffs  $\nu_1 = 10 \text{ MHz}$  and  $\nu_2 = 100 \text{ GHz}$ . The standard

formula, written with the convention of  $S_\nu \propto \nu^{-\alpha}$ , is given by Miley (1980):

$$B_{\min} = 5.69 \times 10^{-5}$$

$$\left[ \frac{1+k}{\eta} (1+z)^{3+\alpha} \times \frac{S_{\text{vob}} v_{\text{ob}}^\alpha}{\theta_x \theta_y l \sin^{3/2} \phi} \frac{(v_1^{(1/2)-\alpha} - v_2^{(1/2)-\alpha})^{2/7}}{\alpha - (1/2)} \right]^{2/7}, \quad (3)$$

where the surface brightness,  $S_{\text{vob}}$ , is in  $\text{Jy beam}^{-1}$ , all frequencies are in GHz,  $\theta_x$  and  $\theta_y$  are in arcseconds,  $l$  is in  $h^{-1}$  kpc, and  $B_{\min}$  is in  $h^{2/7}$  G. The angles  $\theta_x$  and  $\theta_y$  describe the beam size and are, for a Gaussian beam,  $(\ln 2)^{-1/2}$  times the major and minor full width half-maxima. The average of  $\sin^{-3/2} \phi$  over a sphere is  $(8\pi)^{-1/2} [\Gamma(1/4)]^2 \simeq 2.622$ . The formula is relatively insensitive to the high-frequency cutoff because  $\alpha > 0.5$  for the lobes and bridges of most powerful radio galaxies and quasars.

### 3. THE SAMPLES

In order to apply equation (1) to study the ambient gas density in the vicinity of the lobes of powerful extended radio sources, the minimum energy magnetic field and the lobe propagation velocity must be determined in a consistent manner for as large a sample of radio sources as possible. The samples used were those of LMS89 and LPR92. The LMS89 data have already been used by Daly (1994, 1995a) to estimate  $n_a$ ; the luminosity in directed kinetic energy,  $L_j$ ; the characteristic source size,  $l_*$ ; and other quantities with slightly different methodology from that used here.

The selection criteria imposed on galaxies by LMS89 were  $P_{1.78} > 10^{27} h^{-2} \text{ W Hz}^{-1} \text{ sr}^{-1}$ ,  $S_{1.78} > 10 \text{ Jy}$  and that the sources have large angular extent. Eight of their galaxies had largest angular sizes (LAS)  $> 30'$ , and the other two had LAS  $> 20'$ . Two other sources (3C 27 and 3C 409), both in the zone of avoidance, were classified as galaxies based on radio morphology but lacked optical identifications and redshifts in 1989. 3C 27 has since been identified (Hiltner & Roser 1991) with a galaxy at a redshift of 0.184, which implies that its power is actually well below the  $P_{1.78} > 10^{27} h^{-2} \text{ W Hz}^{-1} \text{ sr}^{-1}$  cut. Neither 3C 27 nor 3C 409 are included in this analysis. LMS89 chose quasars to satisfy  $S_{1.78} > 10 \text{ Jy}$  and to be of large angular extent (all seven had LAS  $> 30'$ ).

LPR92 also selected sources of high power with only three of their nine galaxies falling below  $P_{1.78} = 10^{27} h^{-2} \text{ W Hz}^{-1} \text{ sr}^{-1}$  (one of which only slightly) and one of their five quasars falling slightly below that power. In contrast to LMS89, LPR92 chose sources of small angular extent, with only two of the galaxies and one of the quasars larger than  $20'$ .

Neither the LMS89 nor LPR92 samples are complete samples as discussed by the authors. The combined sample does not form a complete sample, especially considering that, as will be described in the next section, there were a few sources in the combined sample that could not be used. However, the large angular size sample of LMS89 paired with the small angular size sample of LPR92 should enable a reasonably complete composite density profile to be obtained for radii from about  $(25\text{--}250) h^{-1}$  kpc; here, the radius is taken to be the core-hot spot separation when a radio core is present and the separation between the hot spot and the center of the galaxy or quasar when a radio

core is not present. Approximately 2/3 of the sources show some sign of a radio core, usually coincident with the center of the optical galaxy or quasar.

### 4. DATA ANALYSIS

LMS89 and LPR92 estimated magnetic fields and synchrotron ages using slightly different methods. The data are reanalyzed here using the raw data in the papers and the LPR92 FITS (Flexible Image Transport System) images. This ensures consistency of method in determining derived quantities. The FITS images were provided by Guy Pooley (1995).

Each lobe was treated as an independent probe of the source environment. This choice, and the slightly different results that are obtained when averaging the data for the two lobes of each source, are discussed in § 7.8.

The minimum energy magnetic field was measured at two projected distances from the hot spot along the ridge line toward the core (10 and  $25 h^{-1}$  kpc). The field at  $10 h^{-1}$  kpc was used to estimate the lobe pressure and both were used in the aging analysis to estimate the lobe propagation velocity, as described in §§ 4 and 4.1.

Not every source in the combined LMS89 and LPR92 sample could be used. Of the seven quasars in the LMS89 survey, four fell below the  $P_{1.78} > 10^{27} h^{-2} \text{ W Hz}^{-1} \text{ sr}^{-1}$  power cut, and three of those had morphological irregularities such as large sideflows or a lack of an observable bridge that made them unusable. Thus, all 10 galaxies and three quasars above the power cut and one of four quasars below the cut from the LMS89 sample were included in the combined sample.

The LPR92 data suffered larger cuts for a number of reasons. Two sources (3C 294 and 3C 299) were unavailable when the FITS maps were provided to us. In two of the smallest sources (3C 263.1 and 3C 266), the observed bridge did not extend as far as  $10 h^{-1}$  kpc from the hot spot (a problem that eliminated three more sources and one lobe from each of two additional sources at  $25 h^{-1}$  kpc). Three of the remaining lobes had morphology that suggested large sideflows or backflows or other serious departures from classical double morphology. Thus, of the LPR92 data, seven lobes from four galaxies (3C 239, 3C 247, 3C 280, and 3C 289) and six lobes from four quasars (3C 254, 3C 268.4, 3C 270.1, and 3C 275.1) are included in the combined sample at  $10 h^{-1}$  kpc, and five lobes from four galaxies and one lobe from one quasar (3C 254) are included in the combined sample at  $25 h^{-1}$  kpc.

Widths and surface brightnesses at both  $10$  and  $25 h^{-1}$  kpc from the hot spots along the ridge line toward the core were measured directly from the published maps and deconvolved as described in § 4.3. These values were then used to estimate  $B_{\min}$  as described in § 2.1; the two field values are hereafter referred to as  $B_{10}$  and  $B_{25}$ . The injection spectral indices relevant for the  $B_{\min}$  computation (eq. [3]) were taken to be the measured index at the brightest point of the lobe (i.e., the hot spot). As noted by LMS89, four of the hot spots (including both in Cyg A) in their sample have spectral indices that appear to show signs of low-frequency turnover, and we followed their lead in adjusting the values of the spectral index for the north lobe of 3C 68.1 and the west lobe of 3C 268.1 to agree with the higher frequency data of Laing (1981). The index used for the  $B_{\min}$  calculation for Cygnus A was 0.7, the apparent lobe injection index of Carilli et al. (1991) rather than the hot

spot index of 0.5 (LMS89 used 0.6), because the field desired is a lobe field. All the other measured hot spot spectral indices were greater than 0.7, so it is unlikely that the hot spot indices are too low. For the LPR92 sources, measuring the spectral indices in this manner produced values that are slightly higher than the injection indices used therein from Laing & Peacock (1980) but that are consistent with those measured for LMS89. For the range of parameters found in these samples,  $B_{\min}$  is not very sensitive to small errors in the injection index; an absolute error of 0.1 in injection index results in about a 10% error in  $B_{\min}$ .

The minimum energy magnetic fields determined from measurements  $10 h^{-1}$  kpc behind the hot spot ( $B_{10}$ ) were, on average,  $1.5 \pm 0.4$  times greater than those from measurements  $25 h^{-1}$  kpc behind ( $B_{25}$ ). Figure 1 shows the ratio  $B_{10}/B_{25}$  as a function of the ratio  $w_{25}/w_{10}$  in the log-log plane, where  $w$  is the deconvolved source width discussed further in § 4.3. We expect the ratio  $w_{25}/w_{10}$  to be greater than or equal to 1 (because the model is of a bridge that expands behind the hot spot), and indeed this turns out to be the case except for 3C 68.2, a rather poorly resolved source. The point on Figure 1 for 3C 239 is also an outlier; its width at  $25 h^{-1}$  kpc ( $w_{25}$ ) was measured from the 1.4 GHz map but could not be measured on the 5 GHz map. Extrapolation of width measurements on the 5 GHz map would lead to a significantly larger value of  $w_{25}$ . Excluding 3C 68.2 and 3C 239, the data are fitted by a line of slope  $1.46 \pm 0.14$  and intercept  $0.035 \pm 0.018$ . A slope of 4/3 and intercept of zero are predicted if the dominant mechanism determining surface brightness falloff in the bridge is lateral adiabatic expansion, where the lobe magnetic field strength and width are time independent for a given radio source, as is discussed in detail by WDW97 and Wellman & Daly (1996a). This result and those presented by WDW97 suggest a simple model in which the bridge is quiescent with insignificant backflow and insignificant reacceleration of electrons to relativistic energies and undergoes lateral adiabatic expansion. The slightly nonzero intercept is likely the result of slight hot spot contamination of the  $10 h^{-1}$  kpc measurements.

In § 2.1, the appropriate magnetic fields to use in equations (1) and (2) are discussed, and the choices of “lobe field” and “lobe-bridge average,” respectively, are given.

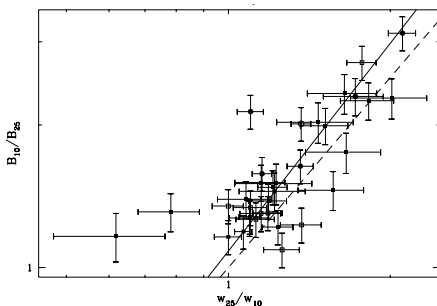


FIG. 1.—Test of expansion. Ratio  $B_{10}/B_{25}$  (the minimum energy magnetic fields estimated 10 and  $25 h^{-1}$  kpc behind the hot spot) as a function of the ratio of the deconvolved widths  $w_{25}/w_{10}$ , in the log-log plane. Circles represent sources from LPR92, and squares represent sources from LMS89. Filled symbols represent galaxy lobes, and open symbols represent quasar lobes. The fitted line (solid) is consistent with that predicted by adiabatic expansion (dashed). The three outliers (the point from 3C 239 and the two points from 3C 68.2) were omitted from the fit and are discussed in § 4.

Taking  $B_{10}$  to be the lobe field and  $B_{25}$  to be the bridge field, the lobe-bridge average was taken to be  $(B_{10} B_{25})^{1/2}$ ; the geometric mean is chosen to give equal statistical weight to the two field estimates and because field estimates in that range of distance from the hot spot generally fall as a power law with distance; thus, the geometric mean is roughly the value at the midpoint. For those sources too short to have a measured  $B_{25}$ , there is generally less distinction between “lobe” and “bridge,” and the bridge field was taken to be  $B_{10}$ . For the source 3C 68.2, which, as noted above, has  $w_{10} > w_{25}$ , it was deemed likely that the poor resolution made the  $10 h^{-1}$  kpc data unreliable, so  $B_{25}$  was used as both bridge and lobe field.

#### 4.1. Ages, Lobe Propagation Velocities, and Ambient Gas Densities

LPR92 estimate the velocity for each lobe by fitting a straight line to the age-distance plot. Ages are derived from break frequencies, assuming a standard method to estimate the minimum energy magnetic field. Break frequencies are derived from spectral indices using the JP spectral model. LPR92 calculate the spectral indices of strips integrated perpendicular to the lobe ridge line and use the whole source index of Laing & Peacock (1980) as the initial index for the JP model.

LMS89 estimate the age of the oldest region detected in each half of each of their sources, assuming a standard method to estimate average minimum energy magnetic fields. The ages on the two sides were generally quite similar as might be expected for symmetric sources such as those in the LMS89 sample. They used the JP model with the observed hot spot index as the initial index. Using the observed hot spot index is equivalent to defining the age to be zero at the hot spot and leads to systematically slightly greater time intervals,  $\Delta t$ , than the LPR92 method by about 10%–15%. From the ages given by LMS89, Daly (1995a) estimated the lobe propagation velocities by measuring the fraction,  $f_D$ , of the lobe-lobe separation,  $D$ , over which radio emission was detected and setting  $v_L = f_D D/2t$ , where  $t$  was taken as the average of the two ages given for each half of the source, (i.e.,  $v_L$  was assumed the same on both sides of the source.) The velocity for Cygnus A obtained by this method agrees well with that obtained by Carilli et al. (1991).

In this paper, the LMS89 and LPR92 data sets are combined and reanalyzed using one consistent method. For the LMS89 sources, ages were calculated from the spectral index slice plots published therein, which were taken along each source’s axis. A length extending from the hot spot as far as the spectral index continued to increase smoothly was chosen and the break frequency at the end of that length was calculated assuming a JP spectrum with initial index equal to the hot spot index. Then, using the lobe-bridge (see § 4) average magnetic field, an age was calculated from equation (2) and a velocity determined by dividing the length by the age. The velocities obtained in this manner for Cygnus A agree very well with the values estimated by Carilli et al. (1991) and Daly (1994, 1995a). This suggests that taking the field for the purposes of aging to be  $(B_{10} B_{25})^{1/2}$  is reasonable.

Using the FITS images of the LPR92 sources, we repeated the aging analysis described in the previous paragraph. Spectral index slices along the sources axes were taken, and the break frequency at the end of a length extending from

the hot spot as far as the spectral index continued to increase smoothly was calculated also assuming a JP spectrum with initial index equal to the hot spot index. Again, the lobe-bridge magnetic field was used in (2) and a velocity determined.

Finally, with lobe minimum energy magnetic fields ( $B_{10}$ ) and velocity estimates for each source, equation (1) is applied to estimate the ambient density in the vicinity of the radio lobe. The results are listed in Table 1 and discussed in §§ 6–8.

Note in equation (2) that for  $B \gg B_{\text{MWB}}$ ,  $t \propto h^{-3/7}$ ,  $v_L \propto h^{-4/7}$  and  $n_a \propto h^{12/7}$ ; for  $B \ll B_{\text{MWB}}$ , then  $t \propto h^{1/7}$ ,  $v_L \propto h^{-8/7}$ , and  $n_a \propto h^{20/7}$ . For  $B \simeq B_{\text{MWB}}$ , which occurs in this sample if there is an offset from minimum energy conditions such as that discussed in § 4.2, the  $h$  dependence is intermediate. Figure 2 shows the ratio  $B_{\text{MWB}}/B_{\text{min}}$  as a function of redshift, where  $B_{\text{min}}$  is the lobe-bridge average.

#### 4.2. Minimum-Energy Magnetic Fields Revisited

An important parameter in the use of the radio properties of powerful extended radio sources to estimate ambient gas densities is the magnetic field strength and total nonthermal pressure of the radio lobe. Equation (1) actually reads  $n_a \propto P_L v_L^{-2}$ , where  $P_L$  is the total pressure of the radio lobe, assumed here to be the nonthermal pressure of the relativistic plasma that gives rise to the observed radio emission from this region. The magnetic field strength and the radio power can be used to estimate  $P_L$  whether or not a source is near minimum energy conditions, and the magnetic field strength enters into the velocity, as discussed in § 2 (see eq. [2]). It is possible that the true magnetic field strength  $B$  is offset from the minimum energy magnetic field  $B_{\text{min}}$  by a factor  $b$ , so that  $B = bB_{\text{min}}$ .

In fact, a comparison of the radio emission with X-rays produced by inverse-Compton scattering of microwave

TABLE 1  
SUMMARY OF SOURCE PROPERTIES

Source	$z$	$r^a$	$a_L^b$	$B_{10}^c$	$B_{25}^c$	$v_L(b=1)^d$	$n_a(b=1)^e$	$v_L(b=1/4)^f$	$n_a(b=1/4)^g$	Map Reference	
3C 55 .....	G	0.720	166	$7.4 \pm 0.6$	$6.4 \pm 0.4$	$4.6 \pm 0.3$	$17 \pm 4$	$0.9 \pm 0.4$	$3.0 \pm 0.7$	$0.5 \pm 0.2$	LMS89
			170	$6.0 \pm 0.8$	$6.5 \pm 0.5$	$4.5 \pm 0.3$	$21 \pm 5$	$0.6 \pm 0.3$	$3.9 \pm 0.8$	$0.3 \pm 0.1$	LM89
3C 68.1 .....	Q	1.238	129	$13.4 \pm 0.7$	$6.6 \pm 0.4$	$4.9 \pm 0.3$	$12 \pm 3$	$2.0 \pm 0.9$	$3.1 \pm 0.6$	$0.5 \pm 0.2$	LMS89
			148	$10.8 \pm 0.6$	$3.4 \pm 0.2$	$2.6 \pm 0.2$	$9 \pm 2$	$1.0 \pm 0.5$	$5 \pm 1$	$0.06 \pm 0.03$	LMS89
3C 68.2 .....	G	1.575	66	$5.2 \pm 1.1$	$7.4 \pm 0.7$	$7.4 \pm 0.7$	$17 \pm 4$	$1.2 \pm 0.8$	$5 \pm 1$	$0.3 \pm 0.2$	LMS89
			73	$5.8 \pm 0.7$	$9.0 \pm 0.6$	$9.0 \pm 0.6$	$17 \pm 4$	$1.8 \pm 0.8$	$3.8 \pm 0.7$	$0.6 \pm 0.2$	LMS89
3C 154 .....	Q	0.580	74	$10.1 \pm 0.4$	$4.0 \pm 0.2$	$3.0 \pm 0.2$	$2.4 \pm 0.6$	$18 \pm 9$	$0.5 \pm 0.1$	$6 \pm 3$	LMS89
			139	$9.3 \pm 0.5$	$2.3 \pm 0.1$	$1.9 \pm 0.1$	$2.3 \pm 0.5$	$7 \pm 3$	$0.8 \pm 0.1$	$0.8 \pm 0.3$	LMS89
3C 175 .....	Q	0.768	104	$12.5 \pm 0.4$	$3.7 \pm 0.2$	$3.4 \pm 0.2$	$5 \pm 1$	$4 \pm 2$	$1.3 \pm 0.2$	$0.9 \pm 0.3$	LMS89
			138	$23.3 \pm 0.7$	$3.0 \pm 0.2$	$2.2 \pm 0.1$	$3.9 \pm 0.8$	$4 \pm 2$	$1.4 \pm 0.2$	$0.5 \pm 0.2$	LMS89
3C 265 .....	G	0.811	158	$6.0 \pm 0.8$	$6.7 \pm 0.5$	$4.4 \pm 0.3$	$12 \pm 3$	$2 \pm 1$	$2.2 \pm 0.4$	$1.0 \pm 0.4$	LMS89
			186	$6.0 \pm 0.8$	$5.4 \pm 0.4$	$2.4 \pm 0.1$	$6 \pm 1$	$5 \pm 2$	$1.7 \pm 0.3$	$1.1 \pm 0.4$	LMS89
3C 267 .....	G	1.144	104	$6.7 \pm 0.6$	$8.5 \pm 0.5$	$4.3 \pm 0.3$	$10 \pm 2$	$5 \pm 2$	$2.2 \pm 0.4$	$1.7 \pm 0.6$	LMS89
			110	$5.5 \pm 0.7$	$10.1 \pm 0.7$	$4.3 \pm 0.3$	$11 \pm 3$	$5 \pm 3$	$2.3 \pm 0.6$	$2 \pm 1$	LMS89
3C 268.1 .....	G	0.974	108	$8.7 \pm 0.4$	$6.1 \pm 0.4$	$4.8 \pm 0.3$	$14 \pm 3$	$1.3 \pm 0.6$	$3.0 \pm 0.6$	$0.5 \pm 0.2$	LMS89
			127	$9.1 \pm 0.4$	$4.8 \pm 0.3$	$4.0 \pm 0.2$	$8 \pm 2$	$3 \pm 1$	$2.0 \pm 0.4$	$0.6 \pm 0.3$	LMS89
3C 322 .....	G	1.681	88	$12.4 \pm 0.6$	$6.8 \pm 0.4$	$4.6 \pm 0.3$	$9 \pm 2$	$3 \pm 1$	$3.7 \pm 0.6$	$0.4 \pm 0.1$	LMS89
			117	$7.2 \pm 0.7$	$10.2 \pm 0.7$	$4.5 \pm 0.3$	$14 \pm 5$	$3 \pm 2$	$5 \pm 2$	$0.6 \pm 0.4$	LMS89
3C 330 .....	G	0.549	128	$6.6 \pm 0.5$	$5.5 \pm 0.3$	$3.6 \pm 0.2$	$12 \pm 3$	$1.4 \pm 0.7$	$2.1 \pm 0.4$	$0.8 \pm 0.3$	LMS89
			132	$6.6 \pm 0.8$	$6.0 \pm 0.4$	$4.2 \pm 0.2$	$13 \pm 3$	$1.5 \pm 0.7$	$2.1 \pm 0.4$	$0.9 \pm 0.3$	LMS89
3C 334 .....	Q	0.555	90	$23.9 \pm 0.7$	$1.7 \pm 0.1$	$1.4 \pm 0.1$	$2 \pm 1$	$3 \pm 3$	$1.2 \pm 0.6$	$0.2 \pm 0.2$	LMS89
			121	$11.9 \pm 0.4$	$3.4 \pm 0.2$	$1.2 \pm 0.1$	$2.8 \pm 0.6$	$9 \pm 4$	$1.0 \pm 0.2$	$1.2 \pm 0.5$	LMS89
3C 356 .....	G	1.079	158	$8.5 \pm 1.3$	$7.7 \pm 0.6$	$3.8 \pm 0.2$	$14 \pm 3$	$2.0 \pm 0.8$	$3.4 \pm 0.6$	$0.6 \pm 0.2$	LMS89
			237	$8.5 \pm 1.3$	$5.6 \pm 0.4$	$3.2 \pm 0.2$	$11 \pm 3$	$1.6 \pm 0.7$	$3.5 \pm 0.6$	$0.3 \pm 0.1$	LMS89
3C 405 .....	G	0.056	44	$7.4 \pm 0.2$	$8.0 \pm 0.5$	$6.3 \pm 0.4$	$5 \pm 1$	$16 \pm 8$	$0.7 \pm 0.2$	$16 \pm 8$	LMS89
			50	$7.4 \pm 0.2$	$7.3 \pm 0.4$	$6.3 \pm 0.4$	$5 \pm 1$	$14 \pm 6$	$0.7 \pm 0.2$	$14 \pm 6$	LMS89
3C 427.1 .....	G	0.572	48	$5.7 \pm 0.4$	$6.3 \pm 0.4$	$4.6 \pm 0.3$	$5 \pm 1$	$11 \pm 5$	$0.8 \pm 0.2$	$7 \pm 3$	LMS89
			53	$8.8 \pm 0.2$	$5.0 \pm 0.3$	$4.2 \pm 0.2$	$3.9 \pm 0.9$	$11 \pm 5$	$0.7 \pm 0.1$	$6 \pm 2$	LMS89
3C 239 .....	G	1.790	44	$6.3 \pm 0.3$	$11.8 \pm 0.7$	$5.5 \pm 0.3$	$17 \pm 5$	$3 \pm 2$	$5 \pm 1$	$0.6 \pm 0.3$	LPR92
3C 247 .....	G	0.749	25	$5.0 \pm 0.5$	$7.0 \pm 0.5$	...	$10 \pm 3$	$3 \pm 2$	$1.6 \pm 0.4$	$2 \pm 1$	LPR92
			41	$3.1 \pm 0.3$	$8.9 \pm 0.6$	$3.9 \pm 0.2$	$7 \pm 2$	$10 \pm 5$	$1.2 \pm 0.3$	$6 \pm 2$	LPR92
3C 254 .....	Q	0.734	39	$6.2 \pm 0.2$	$5.6 \pm 0.3$	$2.8 \pm 0.2$	$6 \pm 2$	$5 \pm 3$	$1.5 \pm 0.4$	$1.5 \pm 0.7$	LPR92
3C 268.4 .....	Q	1.400	34	$4.9 \pm 0.2$	$10.8 \pm 0.6$	...	$38 \pm 19$	$0.5 \pm 0.5$	$7 \pm 3$	$0.3 \pm 0.2$	LPR92
3C 270.1 .....	Q	1.519	28	$4.5 \pm 0.4$	$12.3 \pm 0.8$	...	$33 \pm 14$	$0.9 \pm 0.7$	$6 \pm 2$	$0.5 \pm 0.4$	LPR92
			33	$4.5 \pm 0.4$	$13.7 \pm 0.9$	...	$29 \pm 8$	$1.5 \pm 0.8$	$5 \pm 1$	$0.9 \pm 0.4$	LPR92
3C 275.1 .....	Q	0.557	27	$6.8 \pm 0.3$	$4.8 \pm 0.3$	...	$4 \pm 1$	$8 \pm 5$	$0.7 \pm 0.2$	$5 \pm 3$	LPR92
			41	$4.1 \pm 0.3$	$3.9 \pm 0.2$	...	$4 \pm 1$	$8 \pm 6$	$0.7 \pm 0.2$	$4 \pm 3$	LPR92
3C 280 .....	G	0.996	31	$4.8 \pm 0.3$	$10.5 \pm 0.6$	...	$10 \pm 3$	$8 \pm 4$	$1.5 \pm 0.3$	$6 \pm 3$	LPR92
			38	$4.8 \pm 0.2$	$8.4 \pm 0.5$	$2.7 \pm 0.2$	$4 \pm 1$	$24 \pm 11$	$1.1 \pm 0.2$	$6 \pm 2$	LPR92
3C 289 .....	G	0.967	28	$5.1 \pm 0.3$	$8.7 \pm 0.5$	$5.3 \pm 0.3$	$8 \pm 2$	$8 \pm 3$	$1.5 \pm 0.3$	$4 \pm 1$	LPR92
			29	$5.6 \pm 0.2$	$8.1 \pm 0.5$	$5.2 \pm 0.3$	$7 \pm 2$	$9 \pm 4$	$1.3 \pm 0.2$	$4 \pm 2$	LPR92

<sup>a</sup> Core-hot spot radius in  $h^{-1}$  kpc.

<sup>b</sup> Lobe radius in  $h^{-1}$  kpc.

<sup>c</sup> Minimum energy magnetic field in units of  $h^{2/7} 10 \mu\text{G}$ .

<sup>d</sup> Lobe velocity ( $\times 10^{-2}c$ ) assuming  $B = B_{\text{min}}$ .

<sup>e</sup> Ambient gas density ( $\times 10^{-3} h^{1/2} \text{cm}^{-3}$ ) assuming  $B = B_{\text{min}}$ .

<sup>f</sup> Lobe velocity ( $\times 10^{-2}c$ ) assuming  $B = B_{\text{min}}/4$ .

<sup>g</sup> Electron density ( $\times 10^{-3} h^{1/2} \text{cm}^{-3}$ ) assuming  $B = B_{\text{min}}/4$ .

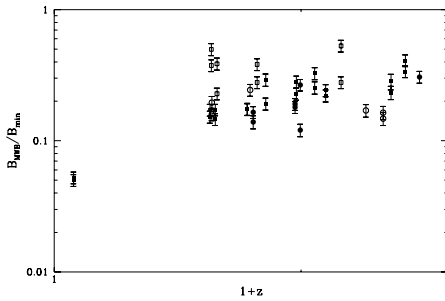


FIG. 2.—Ratio  $B_{\text{MWB}}/B_{\text{min}}$  as a function of redshift, with  $B_{\text{min}}$  given by the lobe-bridge average magnetic field,  $(B_{10} B_{25})^{1/2}$ . Circles represent sources from LPR92, and squares represent sources from LMS89. Filled symbols represent galaxy lobes, and open symbols represent quasar lobes.

background photons with the relativistic electrons that produce the radio emission can be used to estimate the true magnetic field strength  $B$  (see, e.g., Sarazin 1988; Daly 1992a, 1992b to name a few of the many people who have worked on this). This technique has been used to estimate the magnetic field strength in the radio lobes of Fornax A (Feigelson et al. 1995; Kaneda et al. 1995). According to Feigelson et al. (1995),  $b$  is likely to lie between about 0.15 and 0.7 depending on model assumptions.

It has been suggested by Carilli et al. (1991) for the case of Cygnus A, and Perley & Taylor (1991) for the case of 3C 295, that the true magnetic field is a factor of about 3 lower than the minimum energy magnetic field in order for ram pressure confinement of the lobe to be consistent with independent X-ray measurements of the ambient gas density.

We follow the method used by Carilli et al. (1991) and Perley & Taylor (1991) to estimate  $b$  using the strong shock jump conditions across the lobe-medium interface. The equation  $P = 0.75\rho v^2$  allows a determination of  $b$  if there is an independent measure of  $\rho$  since both the nonthermal pressure,  $P = [(4/3)b^{-3/2} + b^2]B_{\text{min}}^2/24\pi$ , and the velocity (see eq. [2]) depend on  $b$ . For Cygnus A,  $\rho \simeq 1.3n_a m_p$  with  $n_a \simeq 0.016 \pm 0.004 h^{1/2} \text{ cm}^{-3}$  from ROSAT observations (Carilli et al. 1994) with the result that  $b \simeq 0.24 \pm 0.02$  averaging over both lobes. Carilli et al. (1991) also show that the value of  $b$  they obtain leads to rough pressure equilibrium of the radio bridge with the ambient gas pressure. Note that Carilli et al. (1991) used an earlier, lower value for the density near Cygnus A, so it is not surprising that there is a slight difference between their result ( $b = \frac{1}{3}$ ) and ours.

We use the two methods mentioned above and a third method to estimate  $b$  in Cygnus A. Two of these methods are independent of the ram pressure argument described above; these are discussed in more detail by WDW97. Two other estimates of  $b$  in Cygnus A are  $b = 0.32 \pm 0.06$ , from the temperature of the ambient gas, and  $b \simeq 0.21 \pm 0.03$ , from pressure equilibrium between the inner bridge and the inner cluster gas (WDW97; Wellman 1996). For the rest of this paper, we will consider the cases  $b = 1$  and  $b = \frac{1}{4}$  with slightly greater emphasis on the latter.

If the true magnetic field strength is indeed a factor of 4 lower than the minimum energy magnetic field, then lobe velocities are reduced by about a factor of 8 for  $bB_{\text{min}} \gg B_{\text{MWB}}$  since  $v_L \propto B^{3/2}$  for  $B \gg B_{\text{MWB}}$  (see eq. [2]). If all the sources satisfied  $bB_{\text{min}} \gg B_{\text{MWB}}$ , there would be no relative effect on the densities derived, but since this is not the case

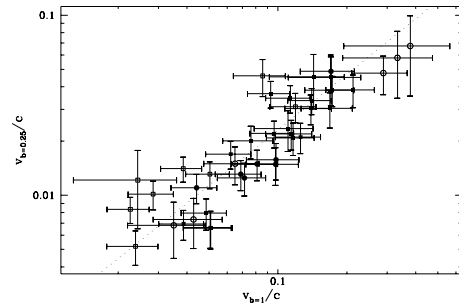


FIG. 3.—Velocities calculated assuming  $B = B_{\text{min}}/4$  as a function of velocities calculated assuming  $B = B_{\text{min}}$ . The linearity of the relation (slope =  $1.02 \pm 0.09$  with a reduced  $\chi^2$  of 1) implies that choosing a somewhat incorrect ratio of  $B$  to  $B_{\text{min}}$  should not greatly effect the results (see also Fig. 4).

here, and since  $v_L$  is not simply scaled by a constant factor when  $B < B_{\text{min}}$ , the values of density will change relative to one another for different values of  $b$ . Figure 2 shows the ratio  $B_{\text{MWB}}/B_{\text{min}}$ . Setting  $b = \frac{1}{4}$  makes  $B_{\text{MWB}}$  comparable to  $bB_{\text{min}}$  in many sources, though not in Cygnus A for which  $bB_{\text{min}}$  is still significantly larger than  $B_{\text{MWB}}$ . Because  $B_{\text{MWB}} \propto (1+z)^2$  (see eq. [2]), the effect of choosing an incorrect ratio of  $B$  to  $B_{\text{min}}$  may cause effects that are systematic with redshift. Ages and velocities were recalculated assuming  $B = B_{\text{min}}/4$ . Figure 3 shows the velocity estimated assuming  $b = 0.25$  as a function of the velocity estimated assuming  $b = 1$ . Figure 4 shows the ratio of these two estimates of the velocity as a function of redshift. The ratio is a weak function of redshift; thus, choosing a value of  $b$  that is slightly incorrect probably will not have a great effect.

An interesting and important question is the source to source dispersion of  $b$ . The results described in § 6 can be used to estimate the dispersion in  $b$  from source to source, which is discussed in § 7.4.

#### 4.3. Deconvolution

Once the low-frequency (injection) spectral index is known for a source, the only directly observed quantities in the equation for  $B_{\text{min}}$  (eq. [3]) are  $S_{\nu_{\text{obs}}}$  and  $l$ ; the cutoffs are, in general, assumed rather than observed. Because the sources are not perfectly resolved, a one-dimensional “deconvolution” was devised to attempt to produce a best guess for the source width and maximum surface brightness

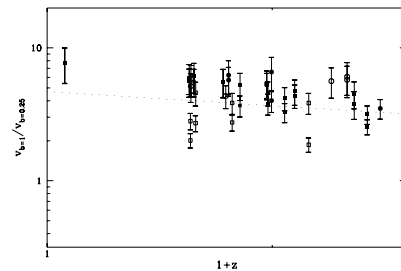


FIG. 4.—Ratio of the velocities assuming  $B = B_{\text{min}}/4$  to the velocities assuming  $B = B_{\text{min}}$  as a function of redshift. The ratio is only a weak function of redshift (slope =  $-0.35 \pm 0.14$  with a reduced  $\chi^2$  of 3.6), so the effect of assuming a somewhat incorrect ratio of  $B$  to  $B_{\text{min}}$  should not be large (see also Fig. 3).

10 (25)  $h^{-1}$  kpc behind the hot spot. The deconvolution is dependent on the assumption that 10 (25)  $h^{-1}$  kpc behind the hot spot, the lobe is well approximated by a cross section of a cylinder with constant volume emissivity and full width  $w_{10}(w_{25})$ . Deviation from this assumption should be more severe at 10 than at 25  $h^{-1}$  kpc. For the rest of this section, duplication replacing “10” with “25” is implicit. This constant emissivity cross section model has the following simple form for the surface brightness through the cross section (prior to convolution with the beam):

$$S_v(10, y) = S_v(10, 0) \sqrt{1 - \left(\frac{2y}{w_{10}}\right)^2},$$

where  $y$  is the projected height from the center line of the bridge. The observed  $S_v$  will be the above convolved with a Gaussian beam. To get the best guess of the true bridge width from the observed width, the maximum surface brightness,  $S_v(10, 0)$ , and the FWHM 10  $h^{-1}$  kpc behind the hot spot were measured and the best guess diameter was taken to be that which, when convolved with a Gaussian of the beam size, gives the observed FWHM. In general, after the “deconvolution,” the width is decreased from its apparent size (typically by 10%–30%) and the peak,  $S_v(10, 0)$ , is increased (typically by 20%–70%) from the value obtained directly from the convolved map. Note that a 70% increase in surface brightness corresponds to only a 15% increase in  $B_{\min}$ . The full width,  $w_{10}$ , equals  $2/(3)^{1/2}$  times the deconvolved FWHM and is twice the lobe diameter. Finally,  $l$  is taken to be  $4w_{10}/\pi$  (random projection; see, e.g., LMS89) and  $S_v(10, 0)$  and  $l$  are inserted into equation (3) to give the minimum energy magnetic field. It should be noted that for most sources, measurements from two different frequency maps, even at differing resolutions, gave the same deconvolved width within error bars. This increases our confidence in the method.

### 5. ERROR ANALYSIS

The measurements of widths and surface brightnesses were made for each lobe and “deconvolved” according to the prescription given in § 4.3. The measurements themselves were made by hand, with a ruler, from the published maps of the two data sets. The initial uncertainties were estimated from the error of measurement with a ruler. The deconvolution procedure included an increase in uncertainty that was a function of how well the width of the source was resolved. The more poorly resolved the source, the larger the uncertainty. Figure 1 served as a check on the errors estimated for  $w$  and  $S$ . Initially, the reduced  $\chi^2$  of the fit in Figure 1 was significantly (almost a factor of 2) lower than 1. As this implied an overestimation of the errors on  $w$  and  $S$ , we scaled those errors down until the reduced  $\chi^2$  of the fit in Figure 1 was equal to 1. As it turned out, the uncertainties described below dominate the determination of errors on velocity and gas density, so scaling the estimated errors on  $w$  and  $S$  has a negligible effect.

Besides the errors on  $w$  and  $S$ , an uncertainty on  $v_T$  (derived from the uncertainty on  $\alpha$ ) is required. LMS89 estimated the maximum error in their determination of spectral index to be 0.1, and regions of sources that had an uncertainty greater than 0.1 were excluded from the analysis. Similarly, when analyzing the FITS images of the LPR92 sources, only regions with an estimated error on the spectral index of less than 0.1 were included. That uncertainty was

propagated through the JP (Jaffe & Perola 1973) spectral model determination of  $v_T$ , which led to errors typically between 10% and 35% on  $v_T$ . For completeness, break frequencies using the Kardachev-Pacholczyk (KP) model (Pacholczyk 1970) were derived, and the two models were found to agree within errors for every source. To obtain the error on the derived quantities ( $B_{10}$ ,  $B_{25}$ ,  $v_L$  and  $n_a$ ), the uncertainties in the observed parameters ( $w_{10}$ ,  $S_{10}$ ,  $w_{25}$ ,  $S_{25}$ ,  $v_T$ , and  $\Delta x$ ) were propagated through the equations defining each derived quantity in terms of the observed parameters.

To try to account for the uncertainty in choosing the correct magnetic field for use in the aging analysis and to account for the nonlinear expansion histories (as mentioned in § 2.1), idealized simulations of aging under different expansion histories were performed to estimate the error arising from these effects. It was estimated that the total error on the derived age was usually less than 20%. It was further estimated that about half that error (14% in quadrature) was a direct result of the effect of adiabatic expansion on the aging process, while the other half was due to the uncertainty in determining the correct magnetic field to use in the age equation (eq. [2]). Thus, a 9% error beyond that from measured quantities was added to the lobe-bridge average magnetic fields (i.e., the fields used to determine the age), and a 14% error was added in quadrature to all ages. The error on  $\Delta x$  was always much smaller than any other error and effectively made no contribution to the overall uncertainty in  $v_L$  or  $n_a$ .

It should be noted that no provision was made for systematic error in the assumptions of the  $B_{\min}$  calculation or the assumption that minimum energy conditions hold except as discussed in §§ 4.2 and 7.4.

### 6. RESULTS

Figures 5 and 6 are log-log plots of  $n_a$  versus core-hot spot separation  $r$  assuming  $b = 1$  and  $b = \frac{1}{4}$ , respectively; see § 4.2 for a discussion of  $b$ . More correctly, these figures are plots of  $(B_{10}/v_L)^2$  versus  $r$ , with a constant of proportionality introduced into equation (1) such that the density of the ambient gas derived at the two lobes of Cygnus A is about  $0.016 h^{1/2} \text{ cm}^{-3}$ , in agreement with *ROSAT* observations (Carilli et al. 1994), which agrees with the ambient gas density estimated via ram pressure confinement when  $b \simeq 0.25$ . Filled symbols represent galaxy lobes, open symbols represent quasar lobes, the data from LPR92

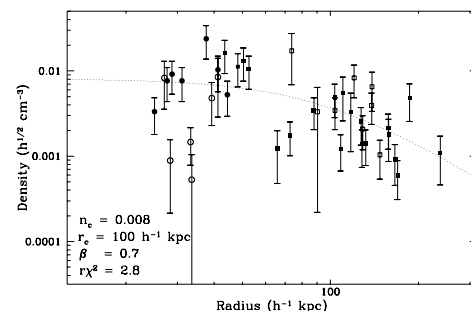


FIG. 5.—Log-log plot of  $n_a$  vs. core-hot spot separation  $r$  assuming minimum energy conditions. Circles represent sources from LPR92, and squares represent sources from LMS89. Filled symbols represent galaxy lobes, and open symbols represent quasar lobes. The King model parameters are those of the best fit, and the best-fit King model is shown.

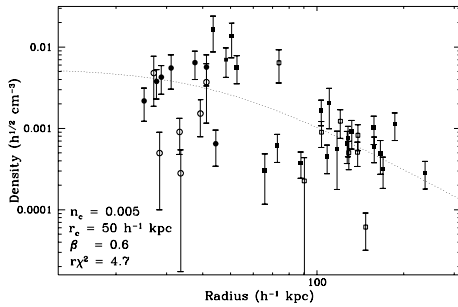


FIG. 6.—Log-log plot of  $n_a$  vs. core-hot spot separation  $r$  assuming  $B = B_{\min}/4$ . Circles represent sources from LPR92, and squares represent sources from LMS89. Filled symbols represent galaxy lobes, and open symbols represent quasar lobes. The King model parameters are those of the best fit, and the best-fit King model is shown.

are represented by circles, and those from LMS89 by squares. Note that many sources have two data points on these figures, one data point from each side of the double-lobed source. As the normalization is to an X-ray measurement, the constant of proportionality varies with  $h$  as  $h^{1/2}$ , which is familiar in X-ray astronomy. Motivated by Daly (1995a, 1995b), who finds the ambient gas to be of cluster-like density and slope, a modified King density profile was fitted to the data and overlaid as the dotted line on the figures. A modified King density profile is given by

$$n_a(r) = n_c \left[ 1 + \left( \frac{r}{r_c} \right)^2 \right]^{-3\beta/2}, \quad (4)$$

where  $n_c$  is the core density and  $r_c$  is the core radius of the gas distribution.

The best-fit parameters are  $n_c = 0.008 h^{1/2} \text{ cm}^{-3}$ ,  $r_c = 100 h^{-1} \text{ kpc}$ , and  $\beta = 0.7$  with a reduced  $\chi^2$  of 2.8 for the  $b = 1$  case and  $n_c = 0.005 h^{1/2} \text{ cm}^{-3}$ ,  $r_c = 50 h^{-1} \text{ kpc}$ , and  $\beta = 0.6$  with a reduced  $\chi^2$  of 4.7 for the  $b = \frac{1}{4}$  case (see Figs. 5 and 6). That the reduced  $\chi^2$ s are greater than 1 is hardly surprising because we are trying to find a composite density profile. Each galaxy is in its own environment, and the degree to which a composite density profile is apparent suggests that the sources inhabit remarkably similar environments. If the source environments were greatly dissimilar, Figures 5 and 6 would be scatter plots with no visible trends. Other effects that could contribute to the  $\chi^2$  include random deviations from minimum energy conditions (discussed in § 7.4), possible off-center location of some sources within their gaseous environments (which are assumed to be spherically symmetric), and evolution of the environments with redshift, as discussed below.

One important question is whether the King model is a better fit than a simple power law. A power-law fit to the data gives  $n_a \propto r^{-0.8}$  with a reduced  $\chi^2$  of 2.9 for the  $b = 1$  case and  $n_a \propto r^{-1.3}$  with a reduced  $\chi^2$  of 4.8 for the  $b = \frac{1}{4}$  case. Hence, there is no significant difference between the power-law and King model fits; we focus on the latter here since it is more physically plausible.

To check for redshift evolution of the density, the sample was split into high- and low-redshift subsamples defined by  $z > 1$  (14 points) and  $z < 1$  (27 points). Figures 7 and 8 (again,  $b = 1$  and  $b = \frac{1}{4}$ , respectively) show the 1 and 2  $\sigma$  confidence regions in the  $n_c$ - $r_c$  plane ( $\beta$  fixed at 0.7, reduced  $\chi^2$  normalized to 1 at the best fit) for fits to the high-redshift (left region) and low-redshift (right region) subsamples. The

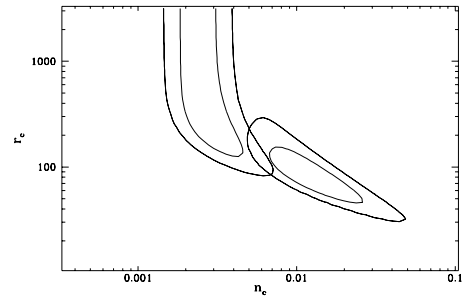


FIG. 7.—One and 2  $\sigma$  confidence regions in the  $n_c$ - $r_c$  plane ( $\beta$  fixed at 0.7, reduced  $\chi^2$  normalized to one at the best fit), for fits to the  $z > 1$  (left region) and  $z < 1$  (right region) subsamples. The small degree of overlap is evidence for evolution of the gas density.

reduced  $\chi^2$ 's before normalization were 1.6 and 2.2 for the high- and low-redshift samples, respectively, in the  $b = 1$  case, and 3.5 and 2.7 for the high- and low-redshift samples, respectively, for the  $b = 0.25$  case. The small overlap of confidence regions suggests evolution of the composite density profile and is significant at about the 2  $\sigma$  level. The placement of the regions suggests two possible forms of evolution with redshift. The first form simply scales core gas density with redshift and assumes no evolution of the core radius and is given by substituting  $n_c = n_{c0}(1+z)^p$  into equation (4). The other form scales core density by the same factor and also scales core radius by  $r_c = r_{c0}(1+z)^{-p/3}$ , thus maintaining constant core gas mass. The first is appropriate if the amount of gas in the core increases with time and the core radius is a constant, the second if the core radius becomes smaller and the core density larger with time such that the core gas mass is time independent, as might be expected if the core is slowly cooling and condensing.

Fits with these two types of evolutionary models are considered for both the  $b = 1$  and  $b = \frac{1}{4}$  cases. In an attempt to determine which of these two evolutionary forms better fits the data, fits allowing independent evolution of gas density and core radius [i.e.  $n_c = n_{c0}(1+z)^p$  and  $r_c = r_{c0}(1+z)^q$ ] were also performed, though these are very poorly constrained given the limited data set studied here. As mentioned in § 7.1, the results of the fit allowing independent evolution of  $n_c$  and  $r_c$  are given in the tables, but the discussion and analysis presented here is confined to the constant core gas mass model ( $q = -p/3$ ) and the core density evolution ( $q = 0$ ) model.

Tables 2A and 3A summarize the results of these fits. The corresponding power-law fits are summarized in Tables 2B

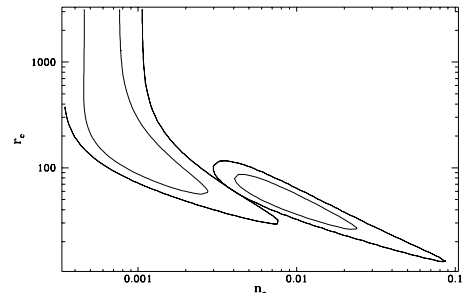


FIG. 8.—One and 2  $\sigma$  confidence regions in the  $n_c$ - $r_c$  plane ( $\beta$  fixed at 0.7, reduced  $\chi^2$  normalized to one at the best fit), for fits to the  $z > 1$  (left region) and  $z < 1$  (right region) subsamples with the assumption that  $B = B_{\min}/4$ .

TABLE 2A

KING MODEL FIT RESULTS WITH  $B = B_{\min}$  AND  $q_0 = 0$ 

$p$	$q$	$n_{c0}^a$	$r_{c0}^b$	$\beta$	$r\chi^2$
$\equiv 0$ .....	$\equiv 0$	8	100	0.7	2.8
-1.7.....	$\equiv 0$	21	110	0.8	2.2
-2.2.....	$\equiv -\frac{1}{3}p$	30	80	1.0	2.1
-2.9.....	1.7	50	40	0.9	2.1

NOTE.—Error estimates are not given in Tables 2A–7A. The reader is referred to the error ellipses in Figs. 14, 15 etc., and to the text.

<sup>a</sup> Core density ( $\times 10^{-3} h^{1/2} \text{ cm}^{-3}$ )

<sup>b</sup> Core radius ( $h^{-1} \text{ kpc}$ ).

TABLE 2B

POWER-LAW FIT RESULTS WITH  $B = B_{\min}$  AND  $q_0 = 0$ 

$p$	$s$	$n_1 \text{ kpc}^a$	$r\chi^2$
$\equiv 0$ .....	$-0.8 \pm 0.1$	110	2.9
-1.7.....	-0.7	280	2.3

NOTE.—Error estimates are not given for the fit  $n_a \propto r^s(1+z)^p$  in Tables 2B–7B. Error ellipses (analogous to those for the King model in Figs. 15 etc.) for these fits are essentially identical for each case studied; the  $1 \sigma$  error contour allows  $p$  to vary by  $\pm 1.7$  and  $s$  to vary by  $\pm 0.6$ . The parameters  $p$  and  $s$  are not strongly correlated.

<sup>a</sup> Density at 1 kpc ( $\times 10^{-3} h^{1/2} \text{ cm}^{-3}$ ).

and 3B. In both Tables 2A and 3A, the evolutionary models are favored over the nonevolutionary model, but there is no significant difference among the three evolutionary models presented. Comparing the two tables, the evolutionary fits in the  $b = \frac{1}{4}$  case have slightly higher reduced  $\chi^2$ , which results from slightly smaller error bars rather than an increase in scatter. The best-fit values for  $\beta$  are moderately lower for  $b = \frac{1}{4}$  (right in the middle of the range of observed  $\beta$ 's for low-redshift clusters), the core radii are smaller, and the power of the implied evolution is greater. The uncertainty in the determination of these fit parameters is discussed in § 6.1. For the reasons given in § 4.2, we will focus on the  $b = \frac{1}{4}$  case. (See Fig. 9 for the fit in the  $b = 1$  case.)

Figure 10 is the same as Figure 6 except that all the densities have been scaled by  $(1+z)^{-p}$  with  $p = -2.9$ , and

TABLE 3A

KING MODEL FIT RESULTS WITH  $B = B_{\min}/4$  AND  $q_0 = 0$ 

$p$	$q$	$n_{c0}^a$	$r_{c0}^b$	$\beta$	$r\chi^2$
$\equiv 0$ .....	$\equiv 0$	5	50	0.6	4.7
-2.9.....	$\equiv 0$	31	50	0.7	2.4
-4.8.....	$\equiv -\frac{1}{3}p$	110	20	0.7	2.3
-4.5.....	1.3	87	20	0.7	2.4

<sup>a</sup> Core density ( $\times 10^{-3} h^{1/2} \text{ cm}^{-3}$ ).

<sup>b</sup> Core radius ( $h^{-1} \text{ kpc}$ ).

TABLE 3B

POWER-LAW FIT RESULTS WITH  $B = B_{\min}/4$  AND  $q_0 = 0$ 

$p$	$s$	$n_1 \text{ kpc}^a$	$r\chi^2$
$\equiv 0$ .....	$-1.3 \pm 0.1$	320	4.8
-2.9.....	-1.3	1800	2.5

<sup>a</sup> Density at 1 kpc ( $\times 10^{-3} h^{1/2} \text{ cm}^{-3}$ ).

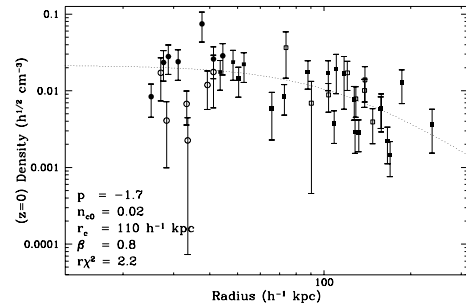


FIG. 9.—Same as Fig. 5 with all densities scaled by  $(1+z)^{-p}$ ; the best-fit  $p$  and King model parameters for the constant core radius evolutionary model are given. The overlaid curve corresponds to those parameters.

the overlaid King model is obtained using the core density evolution model, with the parameters listed in the second row of Table 3A. Comparison with Figure 6 shows the improvement in fit quality given by allowing evolution.

A power-law density fit with core density evolution [i.e.,  $n_a \propto (1+z)^p r^s$ ] gives  $s = -1.3$  and  $p = -2.9$ . The reduced  $\chi^2$  is 2.5.

Another important question to ask is whether some systematic flaw in the analysis is producing the density profile as an artifact. Arguing against that idea, log-log plots of the minimum energy magnetic fields,  $B_{10,25}$ , versus core-hot spot separation (Figs. 11 and 12) and lobe velocity  $v_L$ , obtained assuming  $b = \frac{1}{4}$ , versus core-hot spot separation (Fig. 13) show much larger scatter than the  $n_a$  plots. The dominant error contribution to  $n_a$  is from  $v_L$ , so the difference between the reduced  $\chi^2$  of 8.5 in Figure 13 and the

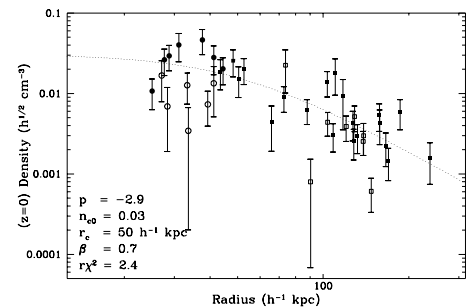


FIG. 10.—Same as Fig. 9 [i.e., a log-log plot of  $n_a$  vs. core-hot spot separation  $r$ , all densities scaled by  $(1+z)^{-p}$ ; the best-fit  $p$  and King model parameters for the constant core radius evolutionary model are given] with the assumption that  $B = B_{\min}/4$ .

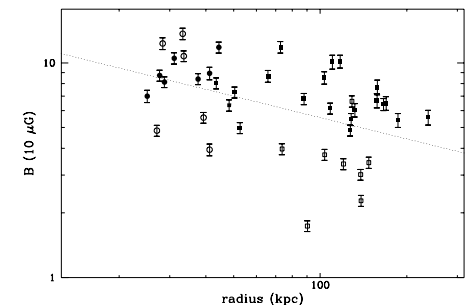


FIG. 11.—Log-log plot of  $B_{10}$  vs. core-hot spot separation. The best straight-line fit is overlaid and has a slope of  $-0.33 \pm 0.02$  with a reduced  $\chi^2$  of 48.

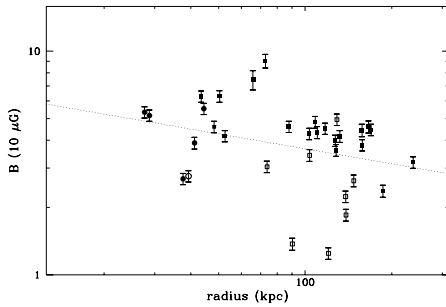


FIG. 12.—Log-log plot of  $B_{25}$  vs. core-hot spot separation. The best straight-line fit is overlaid and has a slope of  $-0.22 \pm 0.02$  with a reduced  $\chi^2$  of 45.

much lower reduced  $\chi^2$ 's in the power-law density fits (4.8 or lower) shows that the density derived from  $B$  and  $v_L$  is more significantly a function of radius than  $B$  or  $v_L$  are separately. No observed or derived quantity shows as clear a trend with radius as does the density.

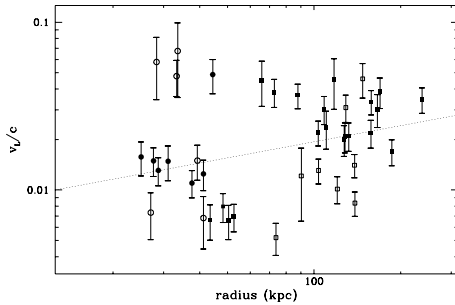


FIG. 13.—Log-log plot of  $v_L$  vs. core-hot spot separation. The best straight-line fit is overlaid and has a slope of  $0.32 \pm 0.05$  with a reduced  $\chi^2$  of 8.5.

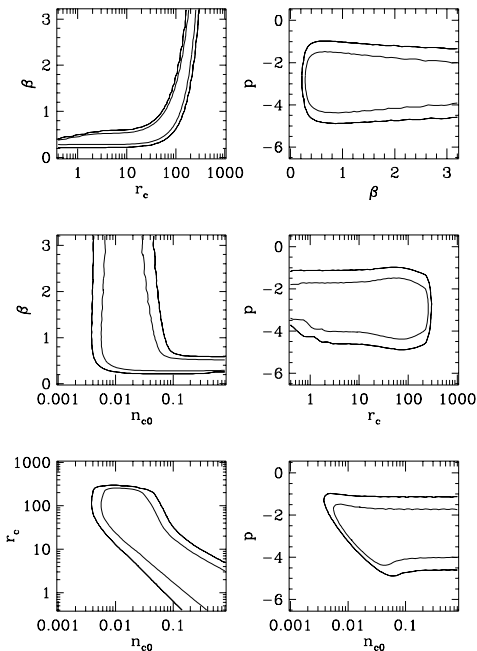


FIG. 14.—Six projections of the four-dimensional error ellipsoid of the parameters fitted to the data with the core density evolution model [eq. (4) with  $n_c = n_{c0}(1+z)^p$ ]. The outer region is  $2\sigma$ ; the inner is  $1\sigma$ . The data do not constrain  $\beta$  well. More data at larger radii would better constrain  $\beta$ .

### 6.1. Errors on the Fit Parameters

A maximum likelihood probability analysis was carried out using the first evolutionary form (and normalizing to a reduced  $\chi^2$  of 1 at the best-fit parameters) and showed that the fit is not well constrained. Figure 14 shows the six projections of the four-dimensional error ellipsoid of the parameters fit. The result for  $b = 1$  is similar with weaker evolution ( $p = 0$  is allowed, although the bulk of the probability implies  $p < 0$ ). The large uncertainty in parameter values is not surprising, given the small number of points. It is likely that more data at radii greater than  $250 h^{-1}$  kpc would tighten the errors on  $r_c$  and  $\beta$  and perhaps the other parameters as well. Results holding  $\beta$  fixed, which have much smaller uncertainties, are discussed in § 7.1.

## 7. DISCUSSION

This study suggests that the density of gas surrounding Cygnus A (Fabbiano et al. 1979; Arnaud et al. 1984; Carilli et al. 1994) is not anomalous compared to other very powerful extended radio sources. In particular, sources the same size as or smaller than Cyg A have ambient gas densities at the radio lobe that are as large as or larger than that in the vicinity of the radio lobes of Cygnus A. Cygnus A is known to be in the core of a cluster of galaxies with an intracluster medium in place, which suggests that these sources inhabit regions of gas whose density and extent can reasonably be explained only if the source is sitting in a gaseous environment like that around Cyg A: i.e., in the gaseous core of a cluster. For example, Jones & Forman (1984) find core densities of low-redshift clusters in the range  $(0.6-40) \times 10^{-3} h^{1/2} \text{ cm}^{-3}$ , which encompasses most of the best-fit core densities derived here. The general symmetry of the sources of all sizes in this sample suggests that each host galaxy is located near the center of a density distribution, just as Cygnus A is near the center of its cluster and density profile. It should be noted that it is only in the case that the sources are located within the gaseous cores of clusters that the derived composite gas density profile reflects the real composite gas density profile, as is argued in this paper. It was once thought that high-redshift radio sources were more asymmetric than low-redshift radio sources. However, McCarthy, van Breugel, & Kapahi (1991) argue that the data are consistent with no evolution of the distribution of source asymmetries with redshift out to redshifts of at least about 1.8.

The values for the ambient gas density in the vicinity of quasars are quite similar to those around radio galaxies. There seems to be somewhat greater scatter about quasars, but the data are consistent with quasars inhabiting regions with the same density profile as radio galaxies. This is consistent with the results of Daly (1995a).

The mass of gas within  $1.5 h^{-1}$  Mpc using the best-fit parameters of the composite density profile obtained assuming  $b = 0.25$  (i.e.,  $n_c = 0.005 h^{1/2} \text{ cm}^{-3}$ ,  $r_c = 50 h^{-1}$  kpc,  $\beta = 0.6$ ) is about  $M_g \simeq 0.6 \times 10^{13} h^{-5/2} M_\odot$  for the nonevolutionary fit. The constant core mass evolutionary fit implies slightly more gas within that radius (about  $1.5 \times 10^{13} h^{-5/2} M_\odot$ ). The core density evolution fit obtained assuming no evolution of the core radius implies a gas mass within  $1.5 h^{-1}$  Mpc of about  $M_g \simeq 3.4 \times 10^{13} h^{-5/2}(1+z)^p M_\odot$ , where  $p$  takes on the best-fit value ( $-2.9$ ). Jones & Forman (1984) find gas masses within a radius of  $1.5 h^{-1}$  Mpc in low-redshift clusters in the range

$(0.5-9) \times 10^{13} h^{-5/2} M_{\odot}$ , a range that encompasses the masses derived from our best fit parameters.

Jones & Forman (1984, § III) divide clusters into two types, those in which the brightest galaxy in the core region is located at the centroid of the X-ray emission (XD clusters) and those in which it is not (nXD clusters). Clusters classified as XD have core radii that typically range from 40 to  $150 h^{-1}$  kpc. Clusters classified as nXD have core radii that typically range from 200 to  $400 h^{-1}$  kpc. The gas mass within a radius of  $1.5 h^{-1}$  Mpc does not seem to be strongly dependent on this classification. The composite density profile derived herein suggests that high-power radio galaxies and quasars tend to inhabit the cores of XD clusters, which suggests that the host galaxy may be the dominant central galaxy itself.

This is consistent with optical observations by Hill & Lilly (1991) of radio galaxies at  $z \simeq 0.5$ . While they did not detect obvious clusters around every radio source, more than half their 3C sources were seen to be in clusters of Abell richness 0 or greater, and in every case that a cluster was detected, the radio emission was associated with the first-ranked cluster member.

### 7.1. Evolution with Redshift

The  $2\sigma$  bound in the  $p$  dimension of the four-dimensional error ellipsoid (Fig. 14) is  $-4.8 < p < -1.0$ , which excludes  $p = 0$ . Nonetheless, it is possible that the chosen form could respond to systematics in the data rather than a real effect. To test this, the nonevolutionary fit (eq. [4]) was run on the  $z < 1$  and  $z > 1$  subsamples separately, holding  $\beta$  fixed at each of three values (0.5, 1.0, and 1.5) as was done in Figure 8 for  $\beta = 0.7$ . In each case, the result was similar to Figure 8—very slight overlap of the outer contours. The placement on the core density axis of the confidence regions corresponding to the high- and low-redshift bins was not dependent on the value of  $\beta$  chosen. Thus, evolution of  $\beta$  is not ruled out but cannot account for the core density evolution required, though evolution of  $\beta$  could mimic or mask evolution of  $r_c$ .

As mentioned in § 6, three forms of evolution were considered, including a fit that allows independent evolution of  $n_c$  and  $r_c$  [i.e., eq. (4) with  $n_c = n_{c0}(1+z)^p$  and  $r_c = r_{c0}(1+z)^q$ ]. This third fit was considered in an attempt to decide which evolutionary model (core density evolution without core radius evolution or constant core gas mass evolution) better describes the data. Unfortunately, the error ellipses generated when fitting this third form are very large (for example, the parameter  $q$  may take on values ranging from  $-2.5$  to  $4.0$ ), so no distinction could be made between the core density (constant core radius) evolution model and the constant core gas mass evolutionary model. The results of the fit allowing independent evolution of  $n_c$  and  $r_c$  are given in each table of King model results, but owing to the large uncertainties allowed by that fit, the analysis and discussion are confined to the constant core gas mass model ( $q = -p/3$ ) and the core density evolution ( $q = 0$ ) model, which are physically plausible and have the virtue of being simple.

The evolution of core gas density implied by the analysis presented here agrees with the results of Wan & Daly (1996a, 1996b) who find that clusters containing FR II's at  $z \simeq 0$  are underluminous in X rays compared to other clusters at  $z \simeq 0$  while clusters containing FR II sources at  $z \simeq 0.5$  may or may not be underluminous in rays com-

pared to other clusters at  $z \simeq 0.5$ . The Wan & Daly (1996a, 1996b) results support the idea that decreasing ICM pressure with increasing redshift allows more FR II sources to inhabit clusters at higher redshift, an idea suggested by Hill & Lilly (1991) and Yee & Green (1987) as a possible explanation for their observation that FR II sources inhabit optically richer environments on average at  $z \simeq 0.5$  than at  $z \simeq 0$ .

Having made the argument that these powerful radio sources lie in the cores of clusters or cluster-like gaseous environments, it can be noted that the King model parameter  $\beta$  for clusters does not take on values as extreme as those allowed by the maximum likelihood analysis (Fig. 14). Typical values for  $\beta$  at low redshift lie in the range 0.6 to 0.8, occasionally as high as 1.0. Accordingly, fits and error ellipses were produced holding  $\beta$  fixed at 0.6 and 1.0. Figure 15 shows the three projections of the three dimensional error ellipsoid obtained when fitting to the core density evolution model [eq. (4) with  $n_c = n_{c0}(1+z)^p$ ] with  $b = \frac{1}{4}$ ,  $\beta$  fixed at 0.6 (left) and 1.0 (right). In each core density–core radius panel, most of the allowed region is consistent with the parameters of XD clusters determined by Jones & Forman (1984). That portion of the allowed region that is not consistent with the parameters determined by Jones & Forman (1984) tends toward greater core density and smaller core radius, which would be consistent with the presence of cooling flows, such as the one seen in Cygnus A (Carilli et al. 1994), in some of the sources. The small core radius, high core density tail explains why a power-law density profile is as good a fit as the King model. Figure 16 shows the three projections of the three-dimensional error ellipsoid when fitting to the constant core mass evolution model [eq. (4) with  $n_c = n_{c0}(1+z)^p$  and  $r_c = r_{c0}(1+z)^{-p/3}$ ] with  $b = \frac{1}{4}$ ,  $\beta$  fixed at 0.6 (left) and 1.0 (right). The allowed regions are similar to those in Figure 15 although the small core radius, large core density tail is greatly exaggerated.

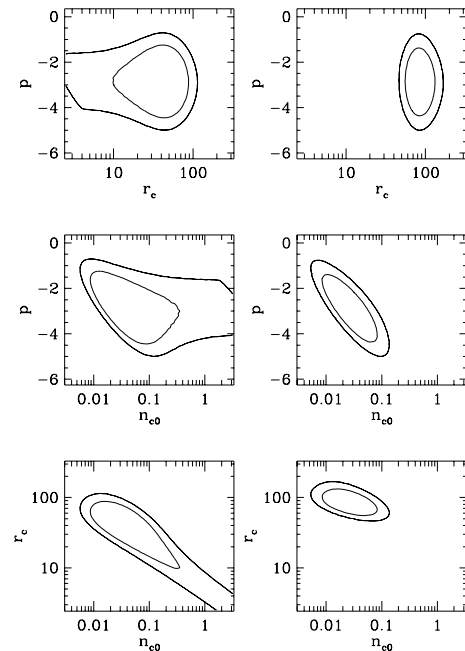


FIG. 15.—Three projections of the three-dimensional error ellipsoid of the parameters fitted to the data with the core density evolution model [eq. (4) with  $n_c = n_{c0}(1+z)^p$ ] with  $\beta$  fixed at 0.6 (left) and 1.0 (right) assuming  $b = \frac{1}{4}$ . The outer region is  $2\sigma$ ; the inner is  $1\sigma$ .

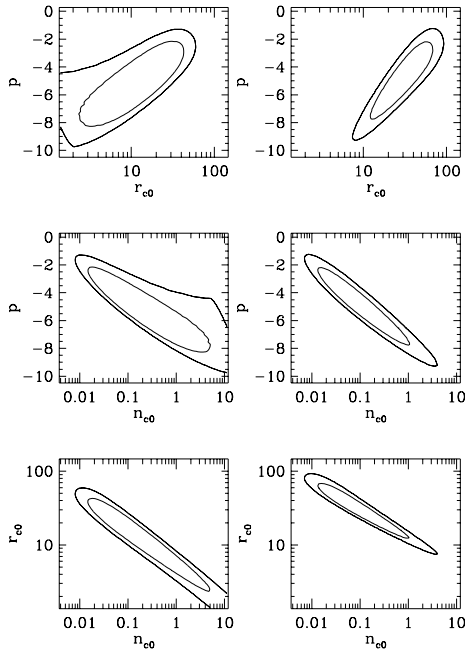


FIG. 16.—Three projections of the three-dimensional error ellipsoid of the parameters fitted to the data with the constant core gas mass evolutionary model [eq. (4) with  $n_c = n_{c0}(1+z)^p$  and  $r_c = r_{c0}(1+z)^{-p/3}$ ] with  $\beta$  fixed at 0.6 (left) and 1.0 (right) assuming  $b = \frac{1}{4}$ . The outer region is  $2\sigma$ ; the inner is  $1\sigma$ . Both this figure and Fig. 15 are discussed in § 7.1.

Again, the presence of this tail reminds us that a power-law density profile is almost as good a fit as the King model. The tail is associated with large values of the evolution parameter  $p$  and is unlikely to represent the true state of affairs. Results for the  $b = 1$  case are similar with weaker implied evolution (compare Tables 2A and 3A).

### 7.2. Selection Effects

The sources in this sample show the usual redshift-power correlation of a flux-limited sample. This raises the concern that any apparent gas density evolution may be an artifact of the flux-limited selection. While it is very difficult to quantify the effect of the redshift-power correlation on apparent gas density evolution, a plot of ambient gas density versus radio power for a fixed redshift should give some indication of such an effect. In particular, if there were a correlation between low density and high radio power at fixed redshift, it would suggest that the apparent gas density evolution is a selection effect arising from the fact that the radio sources are selected from a flux-limited sample and have radio powers that increase with redshift. Figure 17 shows ambient gas density in the vicinity of the lobe as a function of the total radio power of the source for two redshift bins ( $z < 1$ ,  $z > 1$ ). There is no apparent relation between radio power and gas density. Wan & Daly (1996a) also find no relation between radio power and the non-thermal pressure of the bridge—which is likely in near pressure equilibrium with the surrounding gas. This suggests that the observed gas density evolution is not strongly affected by the redshift-power correlation. Another effect that could be considered a selection effect is examined in § 7.6. For a more detailed examination of selection effects, see Wan & Daly (1997).

Another potential selection effect could arise from the limited range of surface brightnesses and spectral indices of

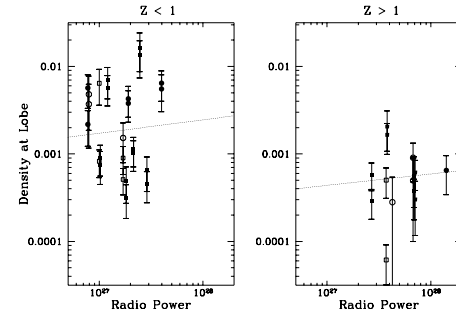


FIG. 17.—Gas density as a function of radio power in the vicinity of the lobe for two redshift bins ( $z < 1$ ,  $z > 1$ ). There is no apparent relation between radio power and gas density at fixed redshift (the slopes of the best-fitting lines are  $0.15 \pm 0.15$  with a reduced  $\chi^2$  of 7.7 and  $0.13 \pm 0.26$  with a reduced  $\chi^2$  of 3.6, respectively), so it is unlikely (§ 7.2) that the redshift-power correlation effects the apparent gas density evolution.

the sources considered here. There is no evidence that such a selection effect is important. First, only a tiny fraction of the sources in the original LMS and LPR samples are not included here owing to limited surface brightness or spectral index coverage (see §§ 3 and 4); note that the LMS89 and LPR92 samples are selected based on total radio power, angular size, and redshift. Second, the lobe propagation velocity is not correlated with any quantity such as the physical length of the bridge over which the aging analysis was conducted or fraction of the total bridge length over which the aging analysis was conducted. Thus, we were unable to identify any hint of a selection effect associated with the surface brightnesses or spectral indices of the sources in the LMS89 and LPR92 samples.

### 7.3. Projection Effects

It is interesting to consider how an ensemble of identical radio galaxies viewed from different angles would appear in this study. In a simplistic treatment, letting  $\theta$  be the angle between the source axis and the plane of the sky, the apparent core-hot spot distance scales as  $\cos \theta$ , as does  $\Delta x$ , the apparent distance over which aging is measured. The line-of-sight depth scales as  $(\cos \theta)^{-1}$ , so the surface brightness scales as  $(\cos \theta)^{-1}$  assuming the brightness is being measured in a fixed physical separation from the hot spot. Hence, the apparent  $B_{\min}$  scales as  $\cos^{-2/7} \theta$ , assuming that the determination of the lobe width is not affected by the projection, and the apparent  $v_L$  scales as  $B_{\min}^{3/2} \Delta x \propto \cos^{4/7} \theta$  for  $B_{\min} \gg B_{\text{MWB}}$ , and  $v_L \sim \Delta x \sim \cos \theta$  for  $B_{\min} \approx B_{\text{MWB}}$ . Thus, the apparent  $n_d$  scales as  $B_{\min}^2/v_L^2 \propto \cos^{-12/7} \theta$  for  $B_{\min} \gg B_{\text{MWB}}$ , or  $\cos^{-18/7} \theta$  for  $B_{\min} \approx B_{\text{MWB}}$ .

A more complex treatment includes the problem that the measurements of surface brightness and width would have been taken 10 (or 25)  $(\cos \theta)^{-1} h^{-1}$  kpc from the hot spot, rather than the fixed physical separation assumed above, which reduces the measured surface brightness and increases the measured width from the values that would be obtained if  $\theta = 0$ . The strength of these effects can be estimated by assuming adiabatic lateral expansion according to an  $a_L \propto (\text{distance from hot spot})^{1/2}$  law; this expansion law and the dependence of surface brightness upon expansion are discussed in WDW97. The prediction of adiabatic lateral expansion for the surface brightness falloff is  $S_\nu \sim a_L^{-4.2}$  for a spectral index,  $\alpha$ , of 0.7. The relations given above indicate that  $a_L \propto \cos^{-1/2} \theta$  and  $S_\nu \sim (\cos \theta)^{-1} a_L^{-4.2}$ , the first term from increased line of sight depth, the second

from lateral expansion. Hence,  $S_v \sim (\cos \theta)^{-1} \cos^{2.1} \theta \sim \cos^{1.1} \theta$ . The apparent minimum energy magnetic field then scales as  $B_{\min} \sim (S_v/a_L)^{2/7} \sim (\cos^{1.1} \theta \cos^{0.5} \theta)^{2/7} \sim \cos^{0.46} \theta$ , and the apparent  $v_L$  scales as  $B_{\min}^{3/2} \Delta x \sim \cos^{0.7} \theta \cos \theta \sim \cos^{1.7} \theta$  for  $B_{\min} \gg B_{\text{MWB}}$ , and  $v_L \sim \Delta x \sim \cos \theta$  for  $B_{\min} \approx B_{\text{MWB}}$ . This leads to apparent  $n_a \propto B_{\min}^2/v_L^2 \sim \cos^{-2.5} \theta$  for  $B_{\min} \gg B_{\text{MWB}}$  and  $n_a \sim \cos^{-1.1} \theta$  for  $B_{\min} \approx B_{\text{MWB}}$ .

The approximate power-law relation between apparent size and ambient density resulting from projection effects is in rough agreement with the slope of the observed density profile, which suggests that projection effects probably do not contribute greatly to the scatter in the density profile. One worry is that it might contribute to the observed profile. There are a few observations that suggest this is not the case. The first is that galaxies and quasars have about the same ambient gas density at a given core-hot spot separation,  $r$ , though they are likely to have rather different values of  $\theta$ . Also, the values of  $r$  have a range of about a factor of 10, whereas projection effects might give a range of a few. Finally,  $r$  in this sample is not strongly dependent on redshift, so that at a given redshift, a fairly broad range of  $r$  is probed. This is expected if the sources have a range of intrinsic lengths and values of  $\theta$ , but it is not expected if the sources all have a similar length  $L$  but a range of  $\theta$ , which follows from the following simple argument. Starting with an ensemble of identical radio galaxies of true length  $L$  randomly oriented with angle  $\theta$  ( $0 < \theta < \pi/2$ ) to the plane of the sky, the probability of  $\theta$  lying between  $\theta'$  and  $\theta' + \delta\theta'$  is  $\cos \theta' \delta\theta'$ . Hence, the probability of the apparent size lying between  $L'$  and  $L' + \delta L'$  is  $L' \delta L' / [L(L^2 - L'^2)^{1/2}]$ . In other words, the apparent sizes would be heavily concentrated toward one size, the true size, rather than evenly spread out, as they are in this sample. Hence, while each of the sources in this sample is likely to be affected to some extent by projection effects, their true sizes are probably distributed as widely as their apparent sizes, and the observed composite density profile is unlikely to be due primarily to projection effects.

#### 7.4. The Dispersion in the Offset from Minimum Energy Conditions

The data presented in § 6 can be used to constrain the dispersion from source to source in the offset from minimum energy conditions. Suppose each source is offset from minimum energy conditions by a different amount so that  $b = B/B_{\min}$  is different for each source and suppose that  $b$  is distributed normally around the average value  $\langle b \rangle$  with standard deviation  $\sigma_b$ . This will contribute a large amount to the scatter in the density as a function of  $r$  since  $n_a$  is a strong function of  $b$ . For example,  $n_a \propto b^{-4.5}$  for  $bB_{\min} > B_{\text{MWB}}$  and  $b < 1$ , which is likely the case for many of the sources considered here. The exact strength of the dependence of  $n_a$  on  $b$  depends on the ratio  $B_{\min}/B_{\text{MWB}}$  and the average value of  $b$  chosen.

To estimate the dispersion in  $b$ , assume all of the sources are in identical environments and that all of the excess scatter in the fit of density to a composite profile is due to the dispersion in  $b$ . First, the contribution of  $\sigma_b/\langle b \rangle$  to the error bar is calculated for each point on the density plots in § 6 and this section. Second, we obtain the value of  $\sigma_b/\langle b \rangle$  that brings the reduced  $\chi^2$  to 1. This yields a very rough estimate of  $\sigma_b/\langle b \rangle$  since if we have (over/under)estimated the other uncertainties contributing to the error on the den-

sities, we will (under/over)estimate  $\sigma_b/\langle b \rangle$ . No doubt there are other contributions to the  $\chi^2$ , for example, from real variations in the source environments. However, since the scatter in the density will be very strongly affected by a dispersion in  $b$ , this does give some indication of how much  $b$  can vary from source to source.

Considering the  $b = \frac{1}{4}$  case (i.e., the data shown in Fig. 10, with fit results in Table 3A),  $\sigma_b/\langle b \rangle$  is less than 0.11 for both models of evolution considered (the constant core gas mass model [ $q = -p/3$ ] and the core density evolution [ $q = 0$ ] model). If the uncertainties on the densities have been overestimated by 50%, then  $\sigma_b/\langle b \rangle$  is still less than 0.14 for both models of evolution. In the  $b = 1$  case (i.e., the data shown in Fig. 9, with fit results in Table 2A),  $\sigma_b/\langle b \rangle$  is less than 0.09 for both models of evolution and is 0.11 if the uncertainties on the densities have been overestimated by 50%.

Hence, this analysis suggests that the acceleration mechanism in these powerful radio sources produces rather close adherence to minimum energy conditions or some particular offset from minimum energy conditions. By itself, this analysis does not favor any particular ratio of  $B$  to  $B_{\min}$ , but it does show that the scatter in  $b$  is likely to be quite small, and as is clear from the fits presented in § 6, similar conclusions are reached for values of  $b$  of 0.25 and 1. At the present time, deviation from minimum energy conditions does seem the most likely way to achieve the appropriate balance of pressures in radio sources; this is discussed in more detail in § 4.2 and by WDW97.

#### 7.5. Effects of the Assumed Cosmology

As mentioned in the Introduction,  $q_0 = 0$  has been assumed when converting angular sizes to physical distances and flux to power. This assumption affects  $\Delta x$  in the calculation of velocity, the line-of-sight depth,  $l$ , in the calculation of  $B_{\min}$  (eq. [3]), as well as the core-hot spot distance. To see whether the results are dependent on this choice, the fit parameters were rederived assuming  $q_0 = 0.5$  for both  $B = B_{\min}$  and  $B = B_{\min}/4$ . The results, summarized in Tables 4A and 5A, are quite similar to those obtained assuming  $q_0 = 0$  except for a modest reduction in the reduced  $\chi^2$  of the nonevolutionary fits and for a modest

TABLE 4A  
KING MODEL FIT RESULTS WITH  $B = B_{\min}$  AND  $q_0 = 0.5$

$p$	$q$	$n_{c0}^a$	$r_{c0}^b$	$\beta$	$r\chi^2$
$\equiv 0$ .....	$\equiv 0$	11	110	1.0	2.4
-1.2.....	$\equiv 0$	23	100	1.0	2.1
-1.5.....	$\equiv -\frac{1}{3}p$	30	80	1.0	2.1
-2.0.....	1.2	42	50	1.0	2.1

<sup>a</sup> Core density ( $\times 10^{-3} h^{1/2} \text{ cm}^{-3}$ ).

<sup>b</sup> Core radius ( $h^{-1} \text{ kpc}$ ).

TABLE 4B  
POWER-LAW FIT RESULTS WITH  $B = B_{\min}$   
AND  $q_0 = 0.5$

$p$	$s$	$n_{1 \text{ kpc}}^a$	$r\chi^2$
$\equiv 0$ .....	$-0.7 \pm 0.1$	100	2.6
-1.2.....	-0.7	260	2.3

<sup>a</sup> Density at 1 kpc ( $\times 10^{-3} h^{1/2} \text{ cm}^{-3}$ ).

TABLE 5A  
KING MODEL FIT RESULTS WITH  $B = B_{\min}/4$   
AND  $q_0 = 0.5$

$p$	$q$	$n_{c0}^a$	$r_{c0}^b$	$\beta$	$r\chi^2$
$\equiv 0$ .....	$\equiv 0$	7	50	0.7	3.8
-2.3.....	$\equiv 0$	34	50	0.7	2.3
-3.8.....	$\equiv -\frac{1}{3}p$	94	20	0.7	2.3
-3.3.....	0.8	62	30	0.7	2.3

<sup>a</sup> Core density ( $\times 10^{-3} h^{1/2} \text{ cm}^{-3}$ ).

<sup>b</sup> Core radius ( $h^{-1} \text{ kpc}$ ).

TABLE 5B  
POWER-LAW FIT RESULTS WITH  $B = B_{\min}/4$   
AND  $q_0 = 0.5$

$p$	$s$	$n_{1 \text{ kpc}}^a$	$r\chi^2$
$\equiv 0$ .....	$-1.1 \pm 0.1$	230	4.0
-2.4.....	-1.2	1500	2.4

<sup>a</sup> Density at 1 kpc ( $\times 10^{-3} h^{1/2} \text{ cm}^{-3}$ ).

reduction in the strength of the redshift evolution of the core density and radius. The corresponding power-law model results are summarized in Tables 4B and 5B. The error ellipses are very similar in size and shape to those shown for the  $q_0 = 0$  case (Figs. 14, 15, and 16). Figures 18 and 19 show the results of the evolutionary fits with  $B = B_{\min}$  and  $B = B_{\min}/4$ , respectively. The best-fit parameters are given in the figures and the data points scaled by  $(1+z)^{-p}$  in the same way as for Figure 9. The flat universe

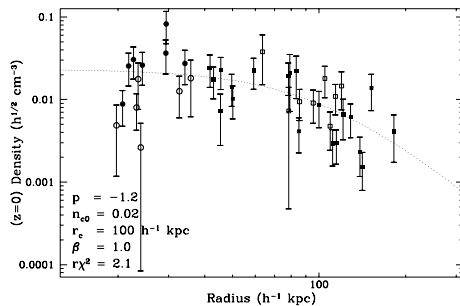


FIG. 18.—Log-log plot of  $n_a$  vs. core-hot spot separation  $r$  under the assumption that  $B = B_{\min}$  and  $q_0 = 0.5$  with all densities scaled by  $(1+z)^{-p}$ ; the best-fit  $p$  and King model parameters for the constant core radius evolutionary model are given. This result is very similar to the  $q_0 = 0$  result (Fig. 9), with weaker implied evolution.

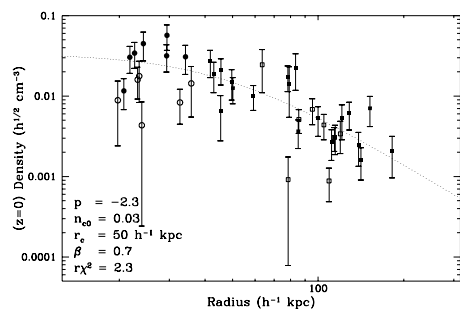


FIG. 19.—Log-log plot of  $n_a$  vs. core-hot spot separation  $r$  under the assumption that  $B = B_{\min}/4$  and  $q_0 = 0.5$  with all densities scaled by  $(1+z)^{-p}$ ; the best-fit  $p$  and King model parameters for the constant core radius evolutionary model are given. This result is very similar to the  $q_0 = 0$  result (Fig. 10), with weaker implied evolution.

cosmology results in a reduction (of roughly 25%–30%) in the strength of the implied evolution, but the  $\chi^2$  was not significantly dependent on the choice of cosmology. Cosmologies with nonzero cosmological constant are left for future work.

### 7.6. Correlation of Spectral Index with Redshift

There is a clear correlation between the spectral indices observed in these sources and redshift. Figure 20 is a log-linear plot of observed hot spot index,  $\alpha_0$ , between 151 MHz and 1.5 GHz for the LMS89 sources and between 1.4 and 5 GHz for the LPR92 sources, as a function of redshift. The overlaid dashed line is the best straight-line fit and has a slope of  $0.8 \pm 0.2$  with a reduced  $\chi^2$  of 1.7. (As in § 5, all spectral indices are taken to have an absolute error of 0.1.) The aged spectral indices (the spectral index at the end of the region used for aging; see § 4.1) show the same correlation with redshift. Thus, the difference between the aged and hot spot (injection) indices shows no correlation with redshift.

One possible cause of this correlation is intrinsic curvature in the injection electron energy spectrum (and therefore in the radio emission spectrum). If the spectrum steepens with frequency, sources at higher redshift will appear to have higher spectral index. Another possibility is that the hot spot spectral index has been affected by inverse-Compton cooling owing to scattering with microwave background photons, which is a very strong function of redshift (see, e.g., Rees & Setti 1968). This would imply that the observed hot spot spectral index is steeper than the true injection spectral index, which is the appropriate index to use to estimate the break frequency in the synchrotron and inverse-Compton cooling estimate of the source ages velocities (see § 2). In either case, the observed spectral index may not be the appropriate index to use to estimate the break frequency, which suggests that the observed spectral index should be corrected for the observed redshift evolution.

The presence of the spectral index–redshift correlation is a concern for any attempt to consider redshift dependence of derived quantities. In particular, the magnitude of the implied gas density evolution (§ 7.1) could be affected. In an attempt to determine how large an effect the spectral index–redshift correlation could have on the magnitude of the implied gas density evolution, magnetic fields, ages, veloci-

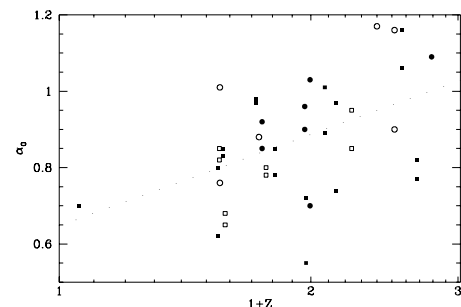


FIG. 20.—Log-linear plot of  $\alpha_0$ , the observed hot spot injection spectral index vs.  $1+z$ . Filled symbols represent galaxy lobes, open symbols represent quasar lobes, the data from LPR92 are represented by circles, and those from LMS89 by squares. The overlaid dashed line is the best straight-line fit and has a slope of  $0.8 \pm 0.2$  with a reduced  $\chi^2$  of 1.7; all spectral indices are taken to have an absolute error of 0.1.

TABLE 6A

KING MODEL FIT RESULTS WITH  $B = B_{\min}/4$ ,  $q_0 = 0$  AND REDSHIFT-CORRECTED  $\alpha$ 'S

$p$	$q$	$n_{c0}^a$	$r_{c0}^b$	$\beta$	$r\chi^2$
$\equiv 0$ .....	$\equiv 0$	9	50	0.6	3.6
-2.1.....	$\equiv 0$	32	50	0.6	2.6
-3.5.....	$\equiv -\frac{1}{3}p$	76	30	0.7	2.5
-3.7.....	1.5	90	30	0.7	2.5

<sup>a</sup> Core density ( $\times 10^{-3} h^{1/2} \text{ cm}^{-3}$ ).  
<sup>b</sup> Core radius ( $h^{-1} \text{ kpc}$ ).

TABLE 6B

POWER-LAW FIT RESULTS WITH  $B = B_{\min}/4$ ,  $q_0 = 0$  AND REDSHIFT-CORRECTED  $\alpha$ 'S

$p$	$s$	$n_1 \text{ kpc}^a$	$r\chi^2$
$\equiv 0$ .....	$-1.2 \pm 0.1$	420	3.7
-2.1.....	-1.2	1400	2.7

<sup>a</sup> Density at 1 kpc ( $\times 10^{-3} h^{1/2} \text{ cm}^{-3}$ ).

ties, and densities were rederived assuming that spectral indices could be corrected to zero redshift using the slope of the correlation in Figure 20. Results assuming  $b = \frac{1}{4}$  are listed in Tables 6A and 7A for  $q_0 = 0$  and  $q_0 = 0.5$ , respectively. The corresponding results for power-law fits are listed in Tables 6B and 7B. The magnitude of the implied gas density evolution is slightly decreased and, while it still appears likely that some evolution is occurring in these sources, the error ellipses (Figs. 21 and 22 for  $q_0 = 0$ ;  $q_0 = 0.5$  is very similar) allow for the possibility of no evolution at  $2 \sigma$  in the case of the redshift correction to the spectral indices.

7.7. Further Discussion

At low redshift, FR I radio sources are typically seen to inhabit moderately rich clusters, where they are often associated with the first-ranked elliptical galaxies, while FR

TABLE 7A

FIT RESULTS WITH  $B = B_{\min}/4$ ,  $q_0 = 0.5$  AND REDSHIFT-CORRECTED  $\alpha$ 'S

$p$	$q$	$n_{c0}^a$	$r_{c0}^b$	$\beta$	$r\chi^2$
$\equiv 0$ .....	$\equiv 0$	11	50	0.7	3.6
-2.0.....	$\equiv 0$	43	40	0.7	2.7
-3.4.....	$\equiv -\frac{1}{3}p$	110	20	0.7	2.6
-4.1.....	1.7	180	20	0.7	2.6

<sup>a</sup> Core density ( $\times 10^{-3} h^{1/2} \text{ cm}^{-3}$ ).  
<sup>b</sup> Core radius ( $h^{-1} \text{ kpc}$ ).

TABLE 7B

POWER-LAW FIT RESULTS WITH  $B = B_{\min}/4$ ,  $q_0 = 0.5$  AND REDSHIFT-CORRECTED  $\alpha$ 'S

$p$	$s$	$n_1 \text{ kpc}^a$	$r\chi^2$
$\equiv 0$ .....	$-1.1 \pm 0.1$	360	3.7
-2.0.....	-1.2	1700	2.8

<sup>a</sup> Density at 1 kpc ( $\times 10^{-3} h^{1/2} \text{ cm}^{-3}$ ).

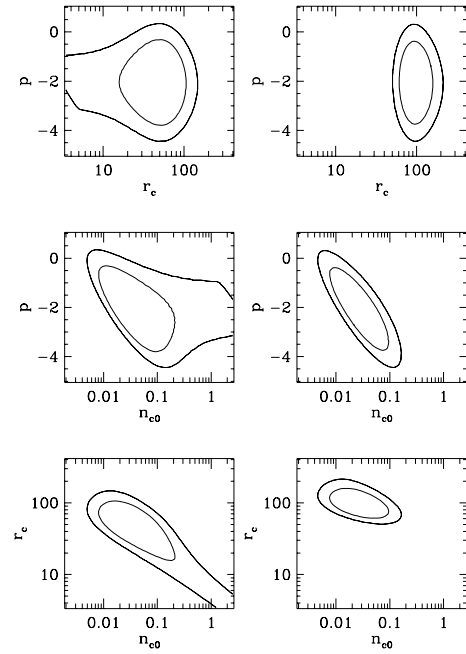


FIG. 21.—Three projections of the three-dimensional error ellipsoid of the parameters fitted to the data with the core density evolution model [eq. (4) with  $n_c = n_{c0}(1+z)^p$ ] with  $\beta$  fixed at 0.6 (left) and 1.0 (right) assuming  $b = \frac{1}{4}$ ,  $q_0 = 0$ , and redshift corrected as discussed in § 7.6. The outer region is  $2 \sigma$ ; the inner is  $1 \sigma$ .

II radio sources are typically seen to be associated with isolated field galaxies or first-ranked members of groups/clusters of sub-Abell richness (see, e.g., Hill & Lilly 1991). At redshifts  $\sim 0.5$ , FR I radio sources inhabit the same cluster

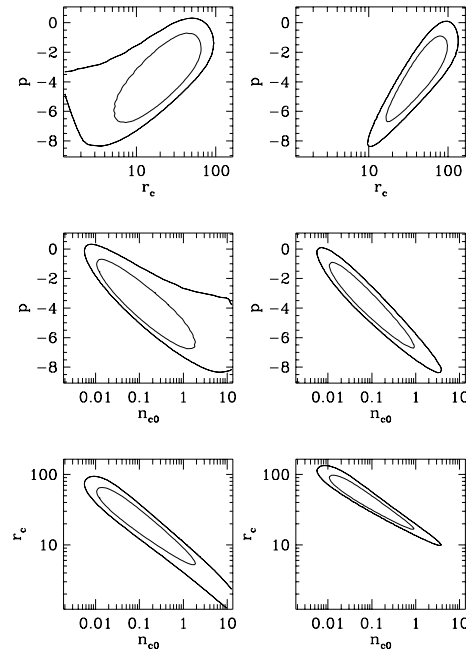


FIG. 22.—Three projections of the three-dimensional error ellipsoid of the parameters fitted to the data with the constant core gas mass evolutionary model [eq. (4) with  $n_c = n_{c0}(1+z)^p$  and  $r_c = r_{c0}(1+z)^{-p/3}$ ] with  $\beta$  fixed at 0.6 (left) and 1.0 (right) assuming  $b = \frac{1}{4}$ ,  $q_0 = 0$ , and redshift corrected as discussed in § 7.6. The outer region is  $2 \sigma$ ; the inner is  $1 \sigma$ .

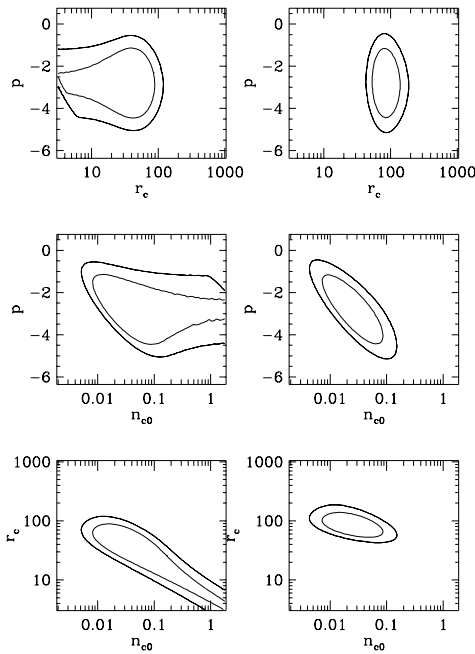


FIG. 23.—Three projections of the three-dimensional error ellipsoid of the parameters fitted to the  $10 h^{-1}$  kpc data with the core density evolution model [eq. (4) with  $n_c = n_{c0}(1+z)^b$ ] assuming  $b = \frac{1}{4}$ , with  $\beta$  fixed at 0.6 (left) and 1.0 (right). Data points for the two lobes of the same source have been averaged. The outer region is  $2\sigma$ ; the inner is  $1\sigma$ . Notice the similarity to Fig. 15, which was produced considering the data from different lobes of the same source to be independent.

environments as they do at low redshift, while the FR II radio sources are found in richer environments on average than at the present. Note that FR II radio sources at redshifts of about 0.5 or less generally have intermediate radio power,  $10^{24} h^{-2} \text{ W Hz}^{-1} \text{ sr}^{-1} < P_{178} < 10^{27} h^{-2} \text{ W Hz}^{-1} \text{ sr}^{-1}$ , and FR II radio sources at redshift greater than about 0.5 generally have very high radio power  $P_{178} > 10^{27} h^{-2} \text{ W Hz}^{-1} \text{ sr}^{-1}$ , and conclusions drawn using intermediate-power FR II radio sources may not apply to very powerful FR II radio sources.

The usual reason postulated for the differing environments for the two morphologies at low redshift is that the higher pressure ICM in richer clusters disrupts the beams and prevents the formation of the FR II morphology except in the case of sources with very high beam power, such as Cygnus A. Following that logic, the change in FR II source environment with redshift implies that either clusters at  $z \sim 0.5$  have a lower pressure ICM than at present or that the typical active galactic nucleus (AGN) at  $z \sim 0.5$  emits more powerful beams than AGNs at present (Hill & Lilly 1991). Of course, both effects may be operating in combination.

Lower pressure ICMs most probably have lower X-ray luminosity because  $P \propto \rho T$  while  $L_X \propto \rho^2 T^{1/2} V$ , where  $P$  is pressure,  $\rho$  is density,  $T$  is temperature,  $L_X$  is X-ray luminosity, and  $V$  is volume. However, current X-ray measurements do not answer the question of cluster gas evolution because there are significant difficulties in unambiguously distinguishing nonthermal core emission from thermal gas emission around radio sources at high redshift with available instruments (see, e.g., Crawford & Fabian 1993, 1995; Worrall et al. 1994; Sokoloski et al. 1996; Wan & Daly

1996a, 1996b). However, the amplitude of the cluster X-ray luminosity function appears to decrease from  $z \simeq 0$  to  $z \simeq 0.4$  (Gioia et al. 1990; Edge et al. 1990; Henry et al. 1992; Bower et al. 1994; Castander et al. 1994), which is consistent with lower pressure ICMs at high redshift.

A study by Wan & Daly (1996a) suggests support for a FR II–low X-ray luminosity connection, finding that at  $z \simeq 0$  clusters containing FR II sources are underluminous in X-rays compared with clusters not containing FR II sources. Crawford & Fabian (1993, 1995) and Worrall et al. (1994) find X-ray emission associated with a number of radio sources including three of the most powerful (3C 356, 3C 289, and 3C 280). Each of these appears to be less X-ray luminous than the Cygnus A cluster and is consistent with negative evolution of ICM pressure and density.

Our apparent detection of negative core density evolution is consistent with, and supportive of, the idea that a decrease in ICM pressure is responsible for the increase in optical richness of typical FR II source environments from low to high redshift. Our analysis extends this trend to higher redshift than previous studies. It is interesting to note that the core density may decrease while the core gas mass remains roughly constant if the core radius increases; this solution is completely consistent with the results presented here.

One other point of interest is that the radio galaxy 3C 220.1 does not appear to be in an optical cluster but is surrounded by enough mass to gravitationally lens as strongly as a cluster (Dickinson 1995). This raises the possibility of gas with an intracluster medium–type density surrounding a galaxy that is in a region that will collapse to a cluster of galaxies in the future but has not yet collapsed; such a picture is reminiscent of the model proposed by Whitmore, Gilmore, & Jones (1993).

#### 7.8. Data Points from the Same Radio Sources

The results for two lobes of one source are not statistically independent in the same way that lobes from different sources are independent because both lobes yield measurements of the gas density in the same potential. In the case of highly symmetric sources, this produces two very similar data points. In Figure 9, there are 41 points, 38 of which are from 19 sources with two measurements. Of those 19 pairs of points, 14 have both members lying on the same side of the fitted line while only five pairs are split by the line. The probability of that many or fewer being split with 19 randomly chosen pairs from those 41 points is small.

Possible sources of asymmetry include asymmetry/clumpiness in the ambient medium, intrinsic beam power asymmetry of the AGN, and off-center location of the host galaxy in the potential. Of the 19 pairs, in eight cases, the lobe that is farther from the core is measured to have a lower ambient density, a result consistent with all sources being well centered in their potentials. Averaging the two results for each source (i.e., plotting average density vs. average radius) seems a reasonable way to get correct statistics and deal with the few sources for which asymmetry is present.

The only real effect of averaging over the two data points for each source is to lower the statistical significance of the results by reducing the number of degrees of freedom; the contribution to the  $\chi^2$  is the same for two nearly identical points as it is for their average because the error bar on the average is smaller by  $2^{1/2}$ . Hence, the contribution to the

reduced  $\chi^2$  doubles. In our case, the reduced  $\chi^2$ 's increased by 50%–60%, which, as less than double, suggests the possibility that some asymmetries in ambient mediums were “averaged out.” Figure 23 shows the three projections of the three-dimensional error ellipsoid when fitting to the core density evolution model [eq. (4) with  $n_c = n_{c0}(1+z)^p$ ] with  $\beta$  fixed at 0.6 (*left*) and 1.0 (*right*) for  $B = B_{\min}/4$ . A comparison of Figure 23 with Figure 15 shows the slight loss of significance. There is a slight reduction in the allowable  $\sigma_b/\langle b \rangle$  described in § 7.4. It is less than 0.11 for  $B = B_{\min}/4$ , even if the original error bars were overestimated by 50%.

It is unclear whether averaging the two points for each source is the statistically correct choice. While the two measurements are in the same potential, they are not “identical” measurements.

## 8. CONCLUSIONS

The composite density profile of powerful extended radio galaxies and quasars derived here from ram pressure arguments appears consistent with density profiles of XD clusters, as described by Jones & Forman (1984); that is, they have core radii and core densities typical of the XD clusters discussed by Jones & Forman (1984) (see § 7). Hence, the host galaxy of the radio emission is probably located in the gaseous core of the cluster and could be the central optically dominant galaxy discussed by Jones & Forman (1984).

The current sample of radio galaxies and quasars extends to a redshift of about 1.8. If, as it appears, all these sources inhabit clusters, there is an implication of early formation of clusters of galaxies. It will be quite interesting to see the ambient gas density in the vicinity of higher redshift, powerful extended radio sources. It appears that there are many sources at higher redshift that could be observed in the radio and used to probe the ambient gas density at very high redshift, which might lead to some interesting conclusions about the evolution of the gas density in the vicinity of the sources. It is unclear how representative the redshift evolution of the gas in the vicinity of these sources is of the evolution of rich environments in general. It may be that these sources are in special (nonrepresentative) environments. A greater worry is that the strong evolution of the radio power with redshift, which is a natural consequence of the selection of the sources from a flux limited survey, biases

the magnetic pressures and lobe propagation velocities that could be detected and thus biases the density that can be detected at any given redshift; this question is currently under detailed investigation by Wan & Daly (1997). The systematic shift of the radio spectral index with redshift and errors, systematic effects, and biases that might be introduced into the velocity estimates by this are also under investigation.

In any case, it does appear that the gas in the vicinity of the sources studied here is undergoing mild evolution with redshift. One explanation of the mild negative evolution of the core gas density with redshift is that powerful extended radio sources are typically located at the base of a region that is slowly cooling and condensing and that the core gas mass is roughly constant; note that cooling times for the gas in the vicinity of the sources and cooling flows about the sources are addressed in detail by WDW97. The sources studied here appear to be in gaseous environments similar to that of Cygnus A, which is known to be at the center of a cooling flow region. Thus, it could be that by studying the redshift evolution of the gaseous environments about radio sources, we are studying the redshift evolution of clusters that have central cooling flows.

The authors would like to thank Mitch Begelman, Roger Blandford, Renyue Cen, Chris Carilli, Dave De Young, George Djorgovski, Ed Groth, Eddie Guerra, Tom Herbig, Jill Knapp, Paddy Leahy, Simon Lilly, Malcolm Longair, Alan Marscher, George Miley, Colin Norman, Jerry Ostriker, Lyman Page, Jim Peebles, Rick Perley, Tony Readhead, Martin Rees, Brigitte Rocca, David Schramm, Rashid Sunyaev, and David Wilkinson for helpful comments and discussions. Special thanks are extended to Robert Lupton for his assistance throughout the data analysis of this work and to Guy Pooley for providing FITS images of the LPR92 sources. It is a special pleasure to thank those involved with the Aspen Center for Physics, which provided a very stimulating environment to present and discuss these results. This work was supported in part by the US National Science Foundation through a National Young Investigator Award, the Natural Sciences and Engineering Research Council of Canada, the Independent College Fund of New Jersey, and by a grant from W. M. Wheeler III.

## REFERENCES

- Alexander, P. 1987, *MNRAS*, 255, 27  
 Alexander, P., & Leahy, J. P. 1987, *MNRAS*, 255, 1  
 Allington-Smith, J. R., Ellis, R. S., Zirbel, E. L., & Oemler, A. 1993, *ApJ*, 404, 521  
 Arnaud, K. A., Fabian, A. C., Eales, S. A., Jones, C., & Forman, W. 1984, *MNRAS*, 211, 981  
 Arnaud, K. A., Johnstone, R. M., Fabian, A. C., Crawford, C. S., Nulsen, P. E. J., Shafer, R. A., & Mushotsky, R. F. 1987, *MNRAS*, 227, 241  
 Begelman, M. C., Blandford, R. D., & Rees, M. J. 1984, *Rev. Mod. Phys.*, 56, 255  
 Begelman, M. C., & Cioffi, D. F. 1989, *ApJ*, 345, L21  
 Bower, R. G., Böhringer, H., Briel, U. G., Ellis, R. S., Castander, F. J., & Couch, W. J. 1994, *MNRAS*, 268, 345  
 Burns, J. O., Gregory, S. A., & Holman, G. D. 1981, *ApJ*, 250, 450  
 Burns, J. O., Rhee, G., Owen, F. N., & Pinkney, J. 1994, *ApJ*, 423, 94  
 Carilli, C. L., Perley, R. A., Dreher, J. W., & Leahy, J. P. 1991, *ApJ*, 383, 554  
 Carilli, C. L., Perley, R. A., & Harris, D. E. 1994, *MNRAS*, 270, 173  
 Castander, F. J., Ellis, R. S., Frenk, C. S., Dressler, A., & Gunn, J. E. 1994, *ApJ*, 424, L79  
 Crawford, C. S., & Fabian, A. C. 1993, *MNRAS*, 260, L15  
 ———. 1995, *MNRAS*, 273, 827  
 Daly, R. A. 1990, *ApJ*, 355, 416  
 ———. 1992a, *ApJ*, 386, L9  
 ———. 1992b, *ApJ*, 399, 426  
 Daly, R. A. 1994, *ApJ*, 426, 38  
 ———. 1995a, *ApJ*, 454, 580  
 ———. 1995b, in *IAU Symp. 168, Examining the Big Bang and Diffuse Background Radiations*, ed. M. Kafatos (Dordrecht: Kluwer), 469  
 Dickinson, M. 1995, private communication  
 Edge, A. C., Stewart, G. C., Fabian, A. C., & Arnaud, K. A. 1990, *MNRAS*, 245, 599  
 Eilek, J. A. 1996, in *ASP Conf. Proc. 100, Energy Transport in Radio Galaxies and Quasars*, ed. P. E. Hardee, A. H. Bridle, & J. A. Zensus (San Francisco: ASP), 281  
 Eilek, J. A., & Arendt, P. N. 1996, *ApJ*, 457, 150  
 Fabbiano, G., Doxsey, R. E., Johnstone, M., & Schwartz, D. A. 1979, *ApJ*, 230, L67  
 Feigelson, E. D., Laurent-Muehleisen, R. I., Kollgaard, R. I., & Fomalont, E. B. 1995, *ApJ*, 449, L149  
 Gioia, I. M., Henry, J. P., Maccacaro, T., Morris, S. L., Stocke, J. T., & Wolter, A. 1990, *ApJ*, 356, L35  
 Henry, J. P., Gioia, I. M., Maccacaro, T., Morris, S. L., Stocke, J. T., & Wolter, A. 1992, *ApJ*, 386, 408  
 Henry, J. P., & Henriksen, M. J. 1986, *ApJ*, 301, 689  
 Hill, G. J., & Lilly, S. J. 1991, *ApJ*, 367, 1  
 Hiltner, P. R., & Roser, H. J. 1991, *A&A*, 244, 37  
 Jaffe, W. J., & Perola, G. C. 1973, *A&AS*, 26, 423  
 Jones, C., & Forman, W. 1984, *ApJ*, 276, 38

- Kaneda, H., et al. 1995, *ApJ*, 453, L13  
 Katz-Stone, D. M., Rudnick, L., & Anderson, M. 1993, *ApJ*, 407, 549  
 Laing, R. A. 1981, *MNRAS*, 195, 261  
 Laing, R. A., & Peacock, J. A. 1980, *MNRAS*, 190, 903  
 Leahy, J. P., Muxlow, T. W. B., & Stephens, P. W. 1989, *MNRAS*, 239, 401 (LMS89)  
 Leahy, J. P., & Williams, A. G. 1984, *MNRAS*, 210, 929  
 Liu, R., Pooley, G., & Riley, J. M. 1992, *MNRAS*, 257, 545 (LPR92)  
 McCarthy, P. J., van Breugel, W., & Kapahi, V. K. 1991, *ApJ*, 371, 478  
 Meyer, S. T., & Spangler, S. R. 1985, *ApJ*, 291, 52  
 Miley, G. 1980, *ARA&A*, 18, 165  
 Morganti, R., Fanti, R., Gioia, I. M., Harris, D. E., Parma, P., & de Ruiter, H. 1988, *A&A*, 189, 11  
 Pacholczyk, A. G. 1970, *Radio Astrophysics* (San Francisco: Freeman)  
 Perley, R. A., & Taylor, G. B. 1991, *AJ*, 101, 1623  
 Pooley, G. 1995, private communication  
 Rees, M. J., & Setti, G. 1968, *Nature*, 219, 127  
 Rudnick, L., & Katz-Stone, D. M. 1996, in *Cygnus A Workshop*, ed. C. Carilli & D. Harris (Cambridge: Cambridge Univ. Press), 158  
 Rudnick, L., Katz-Stone, D. M., & Anderson, M. 1994, *ApJS*, 90, 955  
 Sarazin, C. L. 1988, *X-Ray Emissions from Clusters of Galaxies* (Cambridge: Cambridge Univ. Press)  
 Scheuer, P. A. G. 1995, *MNRAS*, 277, 331  
 ———. 1996, in *ASP Conf. Proc. 100, Energy Transport in Radio Galaxies and Quasars*, ed. P. E. Hardee, A. H. Bridle, & J. A. Zensus (San Francisco: ASP), 333  
 Sokoloski, J. L., Daly, R. A., & Lilly, S. J. 1996, *ApJ*, 459, 142  
 Tribble, P. C. 1993, *MNRAS*, 261, 57  
 Vallée, J. P., & Bridle, A. H. 1982, *ApJ*, 253, 479  
 Wan, L., & Daly, R. A. 1996a, *ApJ*, 467, 145  
 ———. 1996b, in *Cygnus A Workshop*, ed. C. Carilli & D. Harris (Cambridge: Cambridge Univ. Press), 240  
 ———. 1997, in preparation  
 Wellman, G. F. 1996, Ph.D. thesis, Princeton Univ., in preparation  
 Wellman, G. F., & Daly, R. A. 1996a, in *Cygnus A Workshop*, ed. C. Carilli & D. Harris (Cambridge: Cambridge Univ. Press), 215  
 ———. 1996b, in *Cygnus A Workshop*, ed. C. Carilli & D. Harris (Cambridge: Cambridge Univ. Press), 246  
 Wellman, G. F., Daly, R. A., & Wan, L. 1997, *ApJ*, 480, 79 (WDW97)  
 Whitmore, B. C., Gilmore, D. M., & Jones, C. 1993, *ApJ*, 407, 489  
 Worrall, D. M., Lawrence, C. R., Pearson, T. J., & Readhead, A. C. S. 1994, *ApJ*, 420, L17  
 Yates, M. G., Miller, L., & Peacock, J. A. 1989, *MNRAS*, 240, 129  
 Yee, H. K. C., & Green, R. F. 1987, *ApJ*, 319, 28